AN ENERGY APPROACH TO THE DYNAMIC BUCKLING OF SPHERICAL CAPS

Thesis by

Ting-Lung Liu

In Partial Fulfillment of the Requirements

For the Degree of

Aeronautical Engineer

California Institute of Technology

Pasadena, California

1971

(Submitted September 24, 1970)

ACKNOWLEDGMENT

The author wishes to express his deep appreciation to Dr. C. D. Babcock, Jr. for his valuable guidance, advise and encouragement during the course of this work. The helpful suggestion of Drs. E. E. Sechler and D. E. Hudson during the investigation is gratefully acknowledged. Thanks are also due to Drs. M. C. Cheung, and M. El Raheb for their helpful suggestions. Mr. Clarence Hemphill of the Electronic Laboratory, Mr. George Carlson of the Aeronautics Machine Shop and Mr. A. Özkul by their technical assistance have left an indelible mark on this work. Miss Helen Burrus and Mrs. Betty Wood were responsible for typing and figures respectively, and their skillful assistance is gratefully recognized.

This study was supported in part by the Air Force Office of Scientific Research, Office of Aerospace Research, United States Air Force under Grant Number AFOSR 68-1424.

The author also wishes to acknowledge the Fellowship support provided by the Ministry of National Defense of the Republic of China.

ABSTRACT

An experimental study to determine the dynamic buckling load of a spherical cap under impulsive loading was carried out. Impulsive loading was realized experimentally by use of a spray deposited explosive (Silver Acetylide-Silver Nitrate). The experimental dynamic buckling loads were compared to the dynamic buckling loads as calculated by using an energy criterion. The critical load from the energy criterion was determined by the conducting static pressure volume tests on the spherical caps. It was found that experimental results were consistently below the dynamic buckling load as predicted by the energy criterion. It was thought that this inconsistency resulted from the fact that transition state found in the static experiment was not the same as the dynamic transition state.

NOMENCLATURE

A	Area over which surface traction is added
A_i	Coefficient of parabolic line $i = 1, 2, 3$
$\hat{A}$	Area over which explosive is sprayed
b	Base diameter of spherical cap
C	Pendulum Constant $= \dfrac{W}{\sqrt{\ell g}}$
E	Modulus of elasticity $= 10.8 \times 10^6$ psi
g	Gravitational acceleration $= 386$ in/sec^2
H	Vertical displacement of pendulum
h	Local thickness of spherical cap
h_{av}	Average thickness of spherical cap
Δh	Thickness variation of spherical cap
I_p	Impulse
I_{th}	Theoretical impulse
KE	Kinetic energy
ℓ	Length of pendulum system
M	Mass of pendulum system
P	Static preload
$P_{c\ell}$	Classical buckling pressure of complete spherical shell $= \dfrac{2E}{\left[3(1-\nu)^2\right]^{1/2}} \left(\dfrac{h}{R}\right)^2$
P_{EX}	Experimental buckling pressure
P_{EXB}	Experimental buckling pressure before dynamic buckling

NOMENCLATURE (Cont'd)

P_{EXA}	Experimental buckling pressure after dynamic buckling
P_{th}	Theoretical buckling pressure (Ref. 9)
R_i	Local radius of spherical cap
R_{av}	Average radius of spherical cap
S_o	Slope of prebuckling path
S	Slope of postbuckling path
$\overset{\nu}{T}_i$	Surface traction $i = 1, 2, 3$
U	Strain energy
u_i	Displacement of spherical cap $i = 1, 2, 3$
V	Potential energy
$\bar{V}$	Velocity of ballistic pendulum
$\hat{V}$	Velocity of spherical cap
ΔV	Difference of the potential energy
v	Volume
W	Weight of the pendulum
X	Horizontal coordinate of spherical cap
Y	Vertical coordinate of spherical cap
X_o, Y_o	Center of spherical cap
λ	Geometric parameter $= \frac{b}{\sqrt{Rh}} \left[\frac{3}{4}(1 - \nu^2)\right]^{1/4}$
ν	Poisson's ratio $= 0.3$
ρ	Density
ϵ	Round off error

NOMENCLATURE (Cont'd)

α	Postbuckling load deflection angle $= \frac{2}{\pi} \arctan \left(\frac{S}{S_o - S}\right)$
θ	Measurement trace of spherical cap
Δ	Horizontal displacement of pendulum system

LIST OF TABLES

LIST OF FIGURES

LIST OF FIGURES (Cont'd)

LIST OF FIGURES (Cont'd)

TABLE OF CONTENTS

I. INTRODUCTION

Recently, one of the active research areas has been the determination of dynamic buckling criteria through the use of an energy criterion. The attractiveness of this approach to the dynamic buckling problem results from its simplicity.

The analysis for the dynamic buckling of arches with various boundary and loading conditions has been carried out by several investigators (Refs. 1-6). An experimental investigation has been carried out for a clamped arch under step loading (Ref. 4) and an elasticity supported arch with impulsive loading (Ref. 5). The clamped arch subjected to step loading showed good agreement between theory and experiment (Ref. 4). However, for the simply supported arch with an impulsive load the agreement was poor (Ref. 5). The reason for this disagreement is not known at this time. Since the energy approach to the dynamic stability of arches was successful for step loading, the author was encouraged to study a more realistic structure. Therefore, a spherical cap was chosen as a model. This choice was made since a spherical cap has a convenient geometry for experimental work. It was decided to use impulsive loading for the experimental work. However, N. C. Huang's theory (Ref. 7) shows the spherical cap subjected to impulsive load is not a dynamic buckling problem. This is due to the fact that, for the unloaded spherical cap, there exists only one equilibrium position which corresponds to the undeformed position. However, if a static preload is applied, there exist at least three equilibrium positions, if the static preload pressure is above a certain value called the lower buckling pressure.

For each equilibrium position there exists a corresponding potential energy. Therefore, in order for the cap to move from one equilibrium position to another equilibrium position at a given static preloading level, the difference in potential energy must be supplied from an external source. For the impulsive load problem, this energy is supplied in the form of kinetic energy. The critical energy is the minimum amount of energy necessary to go from a lower potential energy state to a higher potential energy state at each static preload.

For the arch problem studied by Cheung (Ref. 4) and Delph (Ref. 5), this amount of energy can be calculated analytically. For the spherical cap, this procedure is very difficult, since the governing equations for this type of problem are highly nonlinear. An attempt is therefore made to determine the potential energy levels directly from the experiment.

Parts II and III of this thesis describes the tests carried out to find the pressure volume behavior of spherical caps under a uniform static pressure and the calculation performed to find the potential energy levels at each static preload. Part IV describes the dynamic buckling tests that were carried out to determine the critical dynamic buckling impulse at several static preload levels. Part V shows the comparison of the dynamic buckling boundary as found from theory and experiment.

It should be emphasized that the work carried out in this thesis is directed toward answering the following two questions:

1. Can the energy barrier between the unbuckled and buckled equilibrium positions be measured experimentally?

2. Is knowledge of the size of this barrier useful in determining the dynamic buckling impulse?

II. STATIC EXPERIMENT

2.1 Cap Design

The geometric parameters of a spherical cap are the thickness, height, and the radius. The ratio of the thickness to the radius of curvature of the middle surface must be much less than one if the spherical cap is to be called "thin". A spherical cap is called "shallow" if the ratio of its rise at the center to the base diameter is less than, approximately 1/8. The static buckling pressure must also be under 15 psi due to limitations in the method of preloading the cap in the dynamic experiments. In addition, the experimental caps were designed such that theoretically two caps had an axisymmetric static buckling mode and two caps had an asymmetric static buckling mode. This fixes the geometric parameter $\lambda = \frac{b}{\sqrt{Rh}} \left[\frac{3}{4}(1-\nu^2)\right]^{1/4}$ to be between 2.5 and 14. With these restrictions, a radius of 20 inches and a base diameter of 4 inches were chosen. This gave a cap thickness varying from 0.015" - 0.030". The caps were machined from 7075-T651 aluminum plate. A drawing of the cap and its integral support is shown in Fig. 1 with the cap mounted in the static test apparatus.

Thickness and radius enter the buckling pressure as squares. Therefore they must be measured as carefully as possible. The thickness was measured many times by using a micrometer. Taking many measurements around the circumference and at the center the average thickness can be calculated. This calculated thickness and the maximum thickness variation are shown in Table I for the four caps tested.

The radius of the caps were determined in the following manner. The spherical cap was measured using a dial gage along each of the following axis: 0^{o}, 45^{o}, 90^{o}, and 135^{o}. The four contours of each spherical cap from the measured data are shown in Figs. 2 through 5. Using a least square method, the data points are fitted by a parabolic polynomial approximation as shown in the figures. This gives the best fit radius for the cap. The theoretical analysis used to determine the radius is shown below:

As shown in Fig. 6 the equation for a circle passing through x, y with radius R is expressed as

$$(X - X_o)^2 + (Y - Y_o)^2 = R^2 \tag{1}$$

The numerical procedure is to find X_o, Y_o and R which best fit the measuring points. Equation (1) can be rearranged as follows:

$$Y = \frac{R^2 - Y_o^2 - (X - X_o)^2}{-2Y_o(1 - \frac{Y}{2Y_o})}$$

since Y_o is approximately equal to R, $\frac{Y}{Y_o} \sim \frac{Y}{R} \sim \frac{0(10^{-1})}{0(10)} \sim 0(10^{-2})$ therefore, by neglecting $0(10^{-2})$

$$Y = \frac{1}{-2Y_o}(R^2 - Y_o^2 - X^2 + 2XX_o - X_o^2) \tag{2}$$

Y can also be expressed as a parabola

$$Y = A_1 + A_2X + A_3X^2 \tag{3}$$

The coefficients A_1, A_2, A_3 are determined by a least square fit

method. Comparing the coefficients of eqs. (2) and (3)

$$A_1 = -\frac{1}{2Y_o}(R^2 - Y_o^2 - X_o^2)$$

$$A_2 = -\frac{X_o}{Y_o} \qquad (4)$$

$$A_3 = \frac{1}{2Y_o}$$

The above equation can be solved for R as follows:

$$R = \sqrt{\frac{1}{4}\left(\frac{A_2}{A_3}\right)^2 + \frac{1}{4}\left(\frac{1}{A_3}\right)^2 - \frac{A_1}{A_3}} \qquad (5)$$

The four radii determined from eq. (5) for each cap and the average radius of each spherical cap is shown in Table II. The estimated error for this procedure is approximately 1 per cent.

2.2 Static Equipment

The pressure-volume behavior of the spherical caps was found using the test equipment shown in Fig. 7. The caps were uniformly pressurized using a hand operated hydraulic oil pump. Since it was desirable to test in a rigid pressure chamber, the pressure was measured using semiconductor strain gages (Kulite DLP-120-500), which were attached on the bottom plate of the pressure chamber. One gage was placed in the tangential direction at the center of the bottom plate and one gage in the radial direction at the edge. They were connected in a half bridge, in such a manner that the signal from the gages added. The voltage across the bridge was maintained at 2.45 volts.

The gages were calibrated using a manometer (Fig. 8). Several runs gave a calibration factor of 3.00 $\pm$ 0.015 psi/mv. After completing the dynamic test (10 months later) this calibration was repeated. At this time the factor was determined to be 2.80 psi/mv. This factor was used in reducing the data after the dynamic tests.

The volume change was measured by a glass tube of constant cross section which was attached on the top side. During the pressure-volume tests the pressure was measured which gave increments in volume of 0.1 inch head. This head was measured using a microscope attached to a traversing mechanism with increments of 0.001 inches. The estimate error in this measuring was less than 3 per cent.

2.3 Static Test Procedure

The pressure-volume experiment was conducted by increasing the pressure gradually, until the load reached the buckling pressure, point A in Fig. 9. At this point the volume changes rapidly to point B in Fig. 9, with an accompanying pressure drop. The location of point B depends upon the ratio of the stiffness of the pressure chamber to the stiffness of the test component. For the pressure-volume tests conducted before the dynamic tests, it was desirable to limit the volume so that the cap experienced no plastic deformation. This was the reason for the rigid pressure chamber. For the pressure-volume tests before the dynamic test, the volume was gradually decreased to some point C in Fig. 9. At this point the spherical cap will snap back to the prebuckling shape point D in Fig.

9. Then with a continuous reduction of the volume head, the pressure will drop to the starting point.

For the post dynamic test experiments, it was necessary to determine the pressure-volume curve to a larger volume than point B. Therefore, after buckling the cap to point B, the volume was increased to point E.

2.4 Static Test Result

The pressure-volume results for spherical caps 1 and 2 are shown in Figs. 11 and 12. Considerable difference in the pre and post test curves is noticed. This results from the damage to the cap occurring during the dynamic test. The consequence of the difference in the pre and post test results in pressure volume behavior will be discussed in the comparison between analysis and experiment.

The pressure-volume behavior after the dynamic tests for spherical caps 3 and 4 were carried out using a large diameter volume tube such that the behavior to point E in Fig. 9 could be determined. The pressure-volume results for caps 3 and 4, pre and post dynamic test are shown in Figs. 13 through 16. The pre and post test results show very little difference in behavior. This indicates little damage was done to the caps during the dynamic tests.

For the four caps tested, the geometric parameter, $\lambda = \frac{b}{\sqrt{Rh}} \left[\frac{3}{4}(1-\nu^2)\right]^{1/4}$, the classical buckling pressure, $P_{c\ell} = (\frac{h}{R})^2 \frac{2E}{[3(1-\nu^2)]^{1/2}}$ and the static buckling pressure for both pre and post dynamic testing are shown in Table III. A comparison is made with the theoretical and experimental results of other

investigators (Refs. 8 and 9) in Fig. 17. As can be seen from the figure, the static buckling pressures before the dynamic tests are very close to the theoretical results except for cap 1. However, this cap gave results similar to other caps of this geometry (Ref. 8). The results after the dynamic tests show that cap 1 and cap 2 suffered damage during the dynamic tests. However, cap 3 and cap 4 buckled at pressures within 1 per cent of the pre dynamic test results.

III. ENERGY CRITERION CALCULATION

The pressure-volume curve from the static experiment can be used to calculate the potential energy of the cap at any pressure level. This is accomplished in the following manner. The potential energy is given as

$$V = U - \int_A \overset{\nu}{T}_i \, u_i \, dA \tag{6}$$

where U is the strain energy and $\int_A \overset{\nu}{T}_i \, u_i \, dA$ is the potential of the applied forces. The surface traction, $\overset{\nu}{T}_i$ can be replaced by the uniform pressure P. For the cap under uniform external pressure, the second term can be expressed as Pv where v is the volume between the deformed and undeformed cap. The strain energy U can be found at any pressure P by determining the work done on the cap up to the pressure and position of interest. This U is given by the integral $\int_o^P Pdv$. Therefore, the potential energy can be written as follows:

$$V = \int_o^P Pdv - Pv \tag{7}$$

With the experimental pressure-volume curve of the spherical caps before (or after) dynamic buckling, eq. (7) can be used to evaluate the potential energy at each pressure level. From these data the energy difference between equilibrium positions at the same value of pressure can be calculated.

Throughout the unstable range, AC, in Fig. 9, the detailed behavior can not be obtained due to the instability of the shell in this

region. Therefore, this part of the pressure-volume relationship is approximate by several curves. A straight line jump and a special curve forming a sharp cusp at the buckling pressure are shown in Figs. 14 through 16. The difference of potential energy caused by these approximations is as much as 18 per cent. This difference will be discussed further in the comparison of the energy criterion with the dynamic test results.

From the experimental pressure-volume curve and eq. (7), the strain energy is obtained by integration along the path from the initial point to the point of interest. The area under the path was obtained using a trapezoidal integration rule. The second term is the multiplication of the pressure and volume at the point of interest. Therefore, the potential energy can be calculated from eq. (7) at each pressure level.

The resulting potential energy curves for the four caps tested are shown in Figs. 18 through 28, both pre and post dynamic test results are shown. At each pressure level between A and B or E (see Fig. 10), there exists at least two equilibrium positions. Each position has a known potential energy.

The equilibrium position on the curve OA has a lower potential energy than the equilibrium position at the same pressure level on the curve AE. The difference in this potential energy represents the minimum increase in energy necessary to cause the cap to buckle. This difference can be easily evaluated from the experimental curves.

IV. DYNAMIC EXPERIMENT

The dynamic experiment consists of applying a short duration impulse loading to the spherical cap. The caps were preloaded by a static external pressure. The response of the cap was measured using a noncontacting displacement pickup. The cap support and pressure chamber were also mounted as a ballistic pendulum in order to determine the impulse delivered to the cap.

4.1 Design of Dynamic Equipment

The static preloading on the cap was applied by partially evacuating a chamber behind the cap. However, since in some tests the static preload was only 2 psi, a shock wave is created in the chamber by the vibrating cap. This phenomena will effect the cap displacement. In order to avoid the interference of the reflecting wave, the length of chamber was chosen to be 20 inches long. This gives 2.5 milliseconds before the reflected shock wave reaches the cap. Since the pressure chamber is part of the ballistic pendulum (Fig. 29), it was necessary to design it with a minimum weight to insure adequate motion of the pendulum. Therefore, a 1/8 inch wall thickness cast acrylic resin tube was selected.

The pickup holder and support (Fig. 31), were designed such that the measurement of the displacement of the spherical cap was not affected by the motion of the pickup itself, and so it gave minimum interference with the shock wave generated by the cap. In order to find some estimate of the pickup support motion, it was assumed that

the pickup was forced with a pressure pulse having the same frequency as the vibrating cap. An approximate natural frequency of the spherical cap of 3,300 cycle/sec was obtained by Galerkin's method.

The noncontacting displacement pickup was mounted at the center of a beam support. The natural frequency and amplitude of supporting system were calculated by Hamilton's principle. The beam was made of steel with a 3/16 inch width and a 1/2 inch height. The pickup holder was made of aluminum, and the estimated natural frequency of the supporting system was approximately 4,200 cycle/sec. The maximum amplitude of the pickup was calculated to be less than 0.001 inches.

4.2 Dynamic Equipment

The impulsive load was generated using a light sensitive spray on explosive (Silver Acetylide-Silver Nitrate, $Ag_2C_2 \cdot A_gNO_3$, Refs. 4 and 12). The impulse produced by the explosive was determined by its weight. The weight-impulse calibration was found during the course of the dynamic experiments. The amount of explosive powder was sprayed on Mylar over a 2 inch diameter circle and weighed by an analytical balance to $\pm$ 0.001 gm. The Mylar was deformed into a spherical shape by a heat treatment in order to obtain a good contact with the spherical cap. The Mylar was attached to the cap by scotch tape and the explosive was then ready for detonation.

The detonation was accomplished by a high intensity light generated by a Xenon flash tube. The Xenon tube was set 10 inches away from the Mylar and connected with a capacitor charged to 5,000

volts. The center displacement of cap was measured by a pickup which was mounted on the supporting system (Fig. 31). The pickup is a reluctance type transducer which makes no contact with the shell surface being measured. The system is capable of detecting displacements of less than 0.001 inch, and has a working range of approximately 0.35 inches. The pickup output was connected to an oscilloscope to record the response. A displacement transducer was used at the rear plate of the ballistic pendulum to determine the displacement of the system. This was displayed on an XY plotter. After a dynamic test, the trace on the XY plotter was read by a traversing mechanism in increments of 1/1000 inches. This horizontal displacement, Δ, of the pendulum system can be converted into impulse as follows: The impulse can be related to the momentum of the ballistic pendulum as

$$I_P = M\bar{V} \tag{8}$$

Equating the kinetic energy of the ballistic pendulum to the potential energy at the top of its swing gives

$$MgH = \frac{1}{2} M\bar{V}^2 \tag{9}$$

The rise in height can be related to the horizontal distance for a small angle of swing as follows:

$$H = \frac{\Delta^2}{2\ell} \tag{10}$$

From eq. (8), (9), and (10), the relation between impulse and the pendulum motion is obtained. $I_P = C \cdot \Delta$ where $C = \frac{W}{\sqrt{\ell g}}$ and $W = Mg$.

The impulse data from the experiment are shown in Fig. 32. Using the least square method, the experimental data were fitted with a straight line which is shown in the figure. The data for cap 3 and 4 are shown in Fig. 33. As can be seen, these data are considerably better due to improvements in the experimental technique. Comparing these two calibration lines there is a difference in slope of 0.93 per cent and 1.89 per cent in intercept at the vertical axis. The calibration lines obtained are somewhat different from that obtained by Cheung (Ref. 4). However, the data for this experiment lie in the range of weight below that investigated by Cheung.

4.3 Dynamic Test Procedure

The amount of explosive powder to be sprayed on the Mylar was estimated from the potential energy results. Twelve to sixteen explosive charges were prepared for each cap. The cap displacement pickup was calibrated before each series of dynamic tests. After checking of the transducer and recording system, Fig. 30, the static preloading was applied to the cap using a vacuum pump. At each static preloaded level, the lightest weight of explosive was first selected. Then gradually the weight of explosive was increased until the dynamic buckling boundary was found. Similarly, the dynamic tests were repeated from a lower to a higher static preload level.

4.4 Dynamic Results

As pointed out in the last section, the dynamic tests were conducted by increasing the amount of explosive applied to the caps.

Several traces of the resulting displacement with increasing explosive weight are shown in Fig. 34. The vertical scale is the voltage from the displacement transducer. The horizontal scale is the time axis. For this scale the upper beam is 1 ms/cm and the lower beam is the same trace on a 0.2 ms/cm time scale. The vertical scale of the lower beam is one-half that of the upper beam.

Four distinct types of behavior can be noted in the figure. If the cap is loaded below the dynamic buckling boundary, the response obtained is very small. Several examples of this type of response are shown in Fig. 34, parts A, C, F, and H. If the cap is loaded above the dynamic buckling impulse, and the static preload is sufficiently high, the cap will jump to the buckled position and oscillate about that position. The cap will remain in the buckled position until the static preload is removed. This type of motion is shown in Fig. 34, D, G, and I. For the third type of motion, the cap will jump to the buckled position but will return to the unbuckled position. This occurs because the buckled equilibrium position is incapable of capturing the cap. The return to the unbuckled position is possible since the energy difference between the buckled equilibrium position and the energy of the unstable state is very small. This type of motion is shown in Fig. 34E.

For the fourth type of motion, the cap jumps to the buckled position, returns to the unbuckled position and on the second oscillation returns and stays at the buckled position. This type of motion is shown in Fig. 34B.

The maximum center displacement of the spherical cap was read from the oscilloscope trace as shown in Fig. 34, using the predetermined calibration curve of the displacement pickup. The impulse was also converted from the amount of explosive weight by the calibration curve (see Section 4.2). Then, the experimental maximum displacement was plotted against impulse for each cap. Several of these curves are shown in Figs. 35 and 36.

If the static preload on the cap was sufficiently high, the critical dynamic buckling boundary was distinct. This type of behavior is shown for cap 1, p = 10 psi, cap 2, p = 10.5 psi. For a small value of the preload, the distinction between the unbuckled case and the buckled case was not as clear. Typical of this behavior is the curve for cap 1, p = 7 psi, cap 3, p = 4 psi, cap 4, p = 2 psi. It is difficult to find the critical impulse for dynamic buckling from these curves when the static preload is small. However, the boundary is somewhat easier to find when all of test data are plotted on one curve for the various static preloads. These curves will be discussed in the next section.

V. COMPARISON OF ENERGY CRITERION AND EXPERIMENTAL RESULTS

The impulse required to add a sufficient amount of kinetic energy to the cap to cause buckling can be calculated from the experimentally determined potential energy curves. The calculation is performed as follows: Assume the explosive is uniformly distributed over an area $\hat{A}$, then the initial velocity can be calculated as

$$\hat{V} = \frac{I_{th}}{\rho h \hat{A}} \tag{11}$$

where ρ = density of spherical cap, 0.1 lb/in^3 for aluminum, $\hat{A}$ = the area over which the explosive is applied, π (1)^2 in^2, h = average thickness of the cap (see Table I). The kinetic energy is then determined

$$KE = \frac{1}{2} \rho h \hat{A} \hat{V}^2 \tag{12}$$

This kinetic energy is equated to the difference of the potential energy which can be found from the static test results. Therefore,

$$KE = \Delta V \tag{13}$$

From eqs. (11), (12), and (13) the theoretical impulse is obtained

$$I_{th} = \frac{\sqrt{h \cdot \Delta V}}{24.8} \tag{14}$$

The impulse can be found at each preload level using either the static test results after or before the dynamic buckling tests. Also, for the unstable region, either the line jump or the special curve forming a sharp cusp can be used.

The results of these calculations for the four caps tested are shown in Figs. 37 through 40. The dotted part of the theoretical curves was obtained by extrapolating the experimental data to lower pressures than were experimentally measured.

Caps 1 and 2 were tested in the initial phase of the experimental program. Unfortunately, cap 1 was subjected to a very high impulse in an initial test before a proper calculation of the explosive was determined. Also, cap 2 was tested at a high static preload before tests at lower static preloads were conducted. These two caps suffered some damage (permanent deformation) as can be seen from the pressure-volume curves (Figs. 11 and 12). The result of this is also reflected in the calculation of the theoretical impulse (see Figs. 37 and 38). When comparing the theoretical result with the experiment it seems reasonable to use the theoretical analysis based upon the post dynamic test results since the damage to caps 1 and 2 occurred early in the dynamic testing.

With the experience gained in testing caps 1 and 2, more successful tests were carried out on caps 3 and 4. These caps were tested starting at lower static preloads and then proceeding to higher static preloads. Little difference between results obtained before and after the dynamic tests of caps 3 and 4 was found, except at high static preloads.

In the four figures (Figs. 37 through 40) the experimental critical dynamic buckling boundary was drawn from the test data. The boundary at low static preloads and high static preloads for the four caps is easy to determine. However, it is more difficult to estimate

the boundary in between these two extremes due to the difficulty of obtaining the desired explosive weights. The theoretical line is a smooth curve, therefore, the part between the extremes is interpolated as a smooth line.

Since the unstable equilibrium path could not be measured experimentally in the pressure-volume tests, some estimate of the behavior in this range must be made to make a comparison with the dynamic test results. An indication of the initial slope of this path can be found from the paper by Fitch (Ref. 13). Fitch calculates the initial postbuckling behavior of shallow spherical caps which buckle into an asymmetric mode. This implies $\lambda > 5.5$. In this reference the initial slope of this path is denoted by S and the slope of the prebuckled path is denoted by S_o. From these two slopes a quantity called α is defined as follows:

$$\alpha = \frac{2}{\pi} \arctan \left(\frac{S}{S_o - S}\right)$$

For cap 3, with $\lambda = 6.0$, the α given by Fitch is -0.61. For the two curves given in Fig. 14, the α is -0.81 for the special curve and -0.38 for the straight line jump. For cap 4, with a $\lambda = 6.7$, the α given by Fitch is -0.50. For the two curves given in Fig. 16, the α is -0.82 for the special curve and -0.45 for the straight line jump. The true curves should lie somewhere in between these two extremes.

Comparing the experimental dynamic buckling boundary with the theory, for cap 1, the experiment is as much as 50 per cent lower than the theoretical results. For cap 2, the theory and experiment

are very close. The experiment for cap 3 is lower than the theory by about 25 per cent at intermediate static preload levels. The experimental curve for cap 4 lies 30 per cent lower than the theory over the complete static preloads. In general the experimental data are lower than the theory.

VI. CONCLUSION

The potential energy barrier which separates the buckled and the unbuckled equilibrium states for a spherical cap was determined using the results of static tests. Knowledge of the size of the energy barrier determines the amount of kinetic energy that must be supplied to the cap to make it buckle. The energy was supplied to the cap by using explosive loading.

The static tests as performed contain an unstable region. The behavior of the test specimen in this region depends on the rigidity of the experimental apparatus and the rigidity of the test specimen. This unstable region was approximated by several curves. For most of the curves the difference in critical impulse was very small. However, if the unstable region was approximated by a curve forming a cusp at the buckling point, a considerable difference was found in the estimated impulse. This difference could be as much as 20 per cent. Therefore, further knowledge of the unstable path is necessary for an accurate determination of the critical impulse using the energy criterion.

For the dynamic buckling experiments carried out, the critical impulse could be determined within a reasonable accuracy. For all caps except cap 2 the experimental boundary was below the theoretical boundary. The difference between the theoretical and experimental boundaries was of sufficient size (25 per cent - 50 per cent) that it could not be attributed to experimental error (< 25 per cent) alone. It is interesting to note that the best agreement between theory and

experiment was obtained for cap 2, for which the unstable region of the static tests was smallest.

The sizeable difference between the theory and experiment may also be explained as follows. The energy barrier as determined from the static experimental tests may not be the smallest barrier between the unbuckled and buckled positions. The static tests were carried out in such a manner that part of the postbuckled region was stable, since the tests were constant volume tests. This may have caused the transition state which was used to determine the energy barrier to always be axisymmetric. Other transition states corresponding to lower energy barriers and perhaps nonaxisymmetric deformation may possibly exist.

The determination of the potential energy of these asymmetric transition states by static experimental tests may not be practical. Therefore, either these unstable equilibrium states must be determined analytically or an improved method must be developed to estimate the potential energy of the transition states using both experimental and analytical techniques.

REFERENCES

1. Hoff, N. J. and Bruce, V. G.: Dynamic Analysis of Laterally Loaded Flat Arches. J. Math. Phy., 32, pp. 276-288, (1954).

2. Simitses, G. J.: Dynamic Snap-Through Buckling of Low Arches and Shallow Spherical Caps. Ph. D. Dissertation, Dept. of Aeronautics and Astronautics, Stanford University (1965).

3. Hsu, C. S.: Equilibrium Configuration of a Shallow Arch of Arbitrary Shape and Their Dynamic Stability Character. Int. J. Mech., 3, pp. 113-136 (1968).

4. Cheung, M. C.: The Static and Dynamic Stability of Clamped Shallow Circular Arches. Ph. D. Dissertation, Dept. of Aeronautics, California Institute of Technology, (1969).

5. Delph, T. J.: The Dynamic Stability under Impulsive Loading of Shallow Arches with Elastic End Restraints. Engineer Dissertation, Dept. of Aeronautics, California Institute of Technology (1969).

6. Cheung, M. C. and Babcock, C. D., Jr.: An Energy Approach to Dynamic Stability of Arches. AFOSR 69-2818 TR, September 1969.

7. Huang, N. C.: Axisymmetric Dynamic Snap-Through of Elastic Clamped Shallow Spherical Shells. AFOSR 68-0469 TR, (Feb. 1968).

8. Krenzke, M. A. and Kiernan, T. J.: Elastic Stability of Near Perfect Shallow Spherical Shells. AIAA J., Vol. 1, No. 12. (December 1963).

9. Huang, N. C.: Unsymmetrical Buckling of Thin Shallow Spherical Shells. J. of Appl. Mechanics, p. 453, (Sept. 1946).

10. Liepmann, H.W. and Roshko, A.: Element of Gasdynamics. p. 64, John Wiley and Sons, (May 1967).

11. Roark, R. J.: Formulas for Stress and Strain. p. 354, McGraw-Hill Book Company, New York, (1965).

12. Nevill, G. E. and Hoese, F. O.: Impulsive Loading Using Sprayed Silver Acetylide-Silver Nitrate. Experimental Mechanics, (Sept. 1965).

13. Fitch, J. R. and Budiansky, B.: The Buckling and Postbuckling Behavior of Spherical Caps Under Axisymmetric Load. AIAA/ASME, (April 1969).

TABLE I

WALL THICKNESS OF CAP

Model Number	Wall Average Thickness h_{av} inches	Thickness Variation Δh inches	Base Diameter b inches
I	0.0317	+0.0030	4.018
		-0.0046	
II	0.0245	+0.0017	4.002
		-0.0013	
III	0.0204	+0.0011	3.998
		-0.0014	
IV	0.0160	+0.0010	4.000
		-0.0010	

TABLE II

RADIUS OF CAP

Model Number	Measurement Trace θ^{o}	Coefficient $A_1 x 10^{-1}$	Coefficient A_2	Coefficient $A_3 x 10^{-1}$	Local Radius R_i inches	Round off Error $\mathcal{E} \times 10^{-6}$	Average Radius R_{av} in.
	0	0.157240	0.149594	-0.258104	19.603	21.318	
	45	0.164709	0.148807	-0.256492	19.725	9.458	
I							19.726
	90	0.185613	0.147648	-0.255199	19.823	13.683	
	135	0.179528	0.148200	-0.256116	19.753	17.400	
	0	0.142462	0.166128	-0.287028	17.673	1584.298	
	45	0.133084	0.166946	-0.288176	17.604	1464.769	
II							17.595
	90	0.148561	0.166897	-0.289181	17.544	1380.152	
	135	0.143733	0.166986	-0.288917	17.560	1325.220	

TABLE II (Cont'd)

RADIUS OF CAP

Model Number	Measurement Trace θ^{o}	Coefficient $A_1 x10^{-1}$	Coefficient A_2	Coefficient $A_3 x10^{-1}$	Local Radius R_i inches	Round off Error $\varepsilon x10^{-6}$	Average Radius R_{av} in.
	0	0.200492	0.159027	-0.274867	18.439	331.823	
	45	0.192520	0.159522	-0.276025	18.362	348.686	
III							18.411
	90	0.179280	0.159844	-0.275478	18.398	407.016	
	135	0.185573	0.159183	-0.274756	18.445	427.296	
	0	0.272650	0.159661	-0.277291	18.287	489.758	
	45	0.282109	0.158734	-0.274368	18.480	379.526	
IV							18.276
	90	0.195820	0.163272	-0.280622	18.073	529.757	
	135	0.268375	0.159927	-0.277626	18.265	499.607	

TABLE III

GEOMETRIC PARAMETERS AND BUCKLING PRESSURE

Model Number	λ	$P_{c\ell}$ psi	P_{EXB} psi	P_{EXA} psi	Ratio of P_{EXB}/P_{th}	Ratio P_{EXA}/P_{th}
I	4.60	33.54	16.40	14.17	0.82	0.71
II	5.50	25.31	19.81	14.60	0.98	0.72
III	5.94	15.82	12.66	12.54	1.03	1.02
IV	6.73	10.33	8.34	8.24	1.03	1.02

λ = Geometric parameter

$P_{c\ell}$ = Classical Buckling Pressure

P_{EXB} = Experimental Buckling Pressure before Dynamic Buckling

P_{EXA} = Experimental Buckling Pressure after Dynamic Buckling

P_{th} = Theoretical Buckling Pressure (Ref. 9)

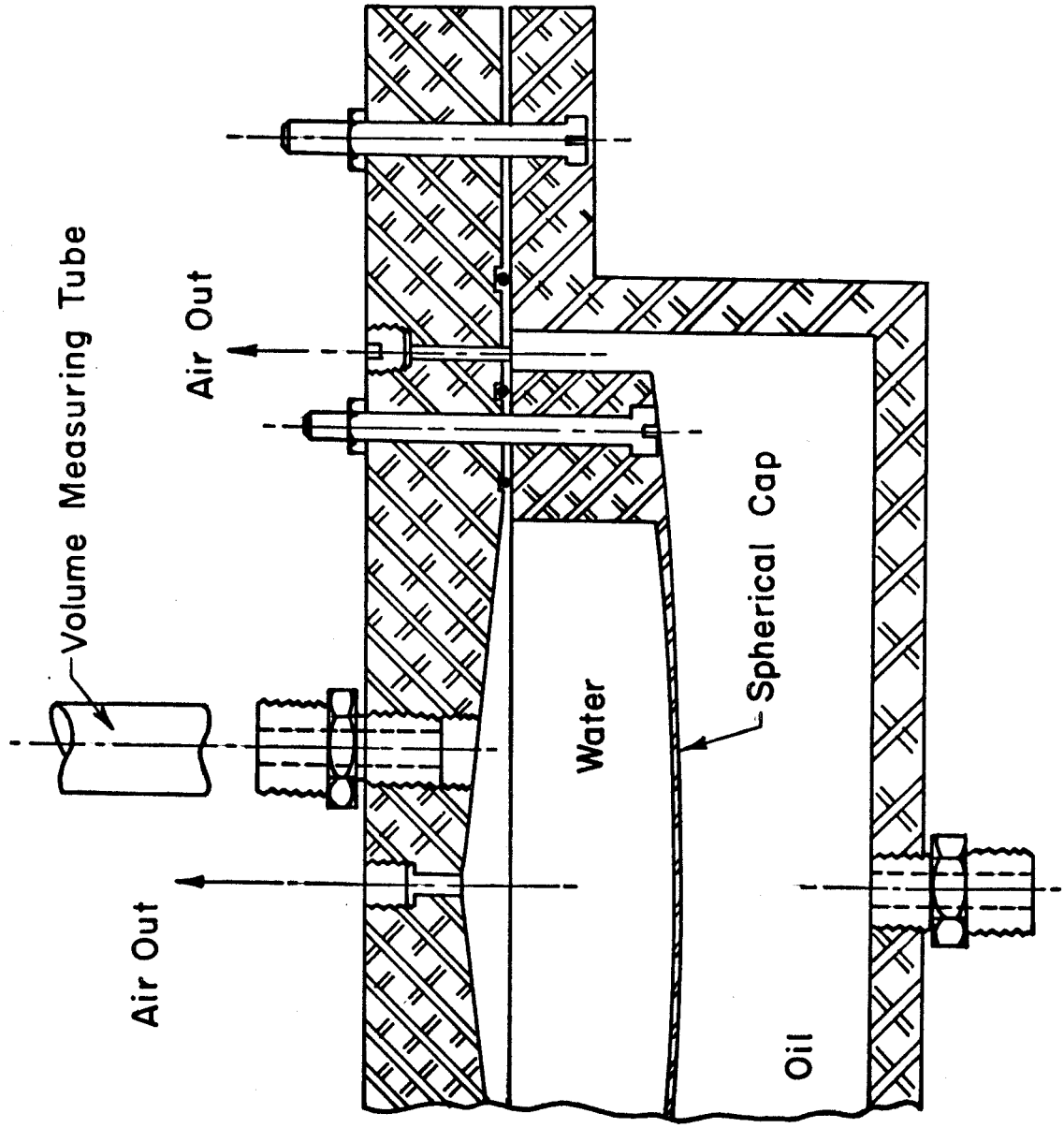

FIG. 1 STATIC TEST APPARATUS

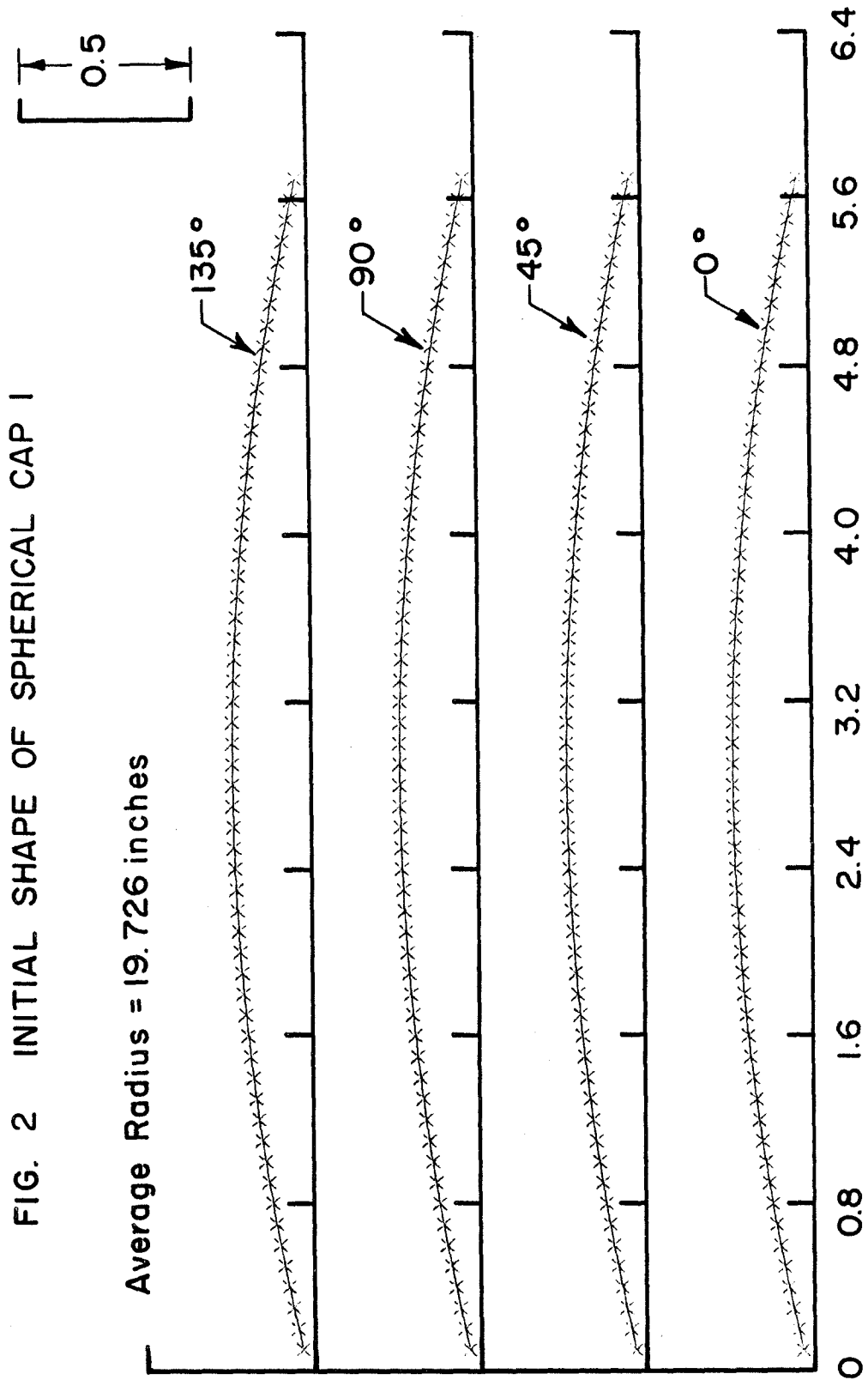

FIG. 2 INITIAL SHAPE OF SPHERICAL CAP I

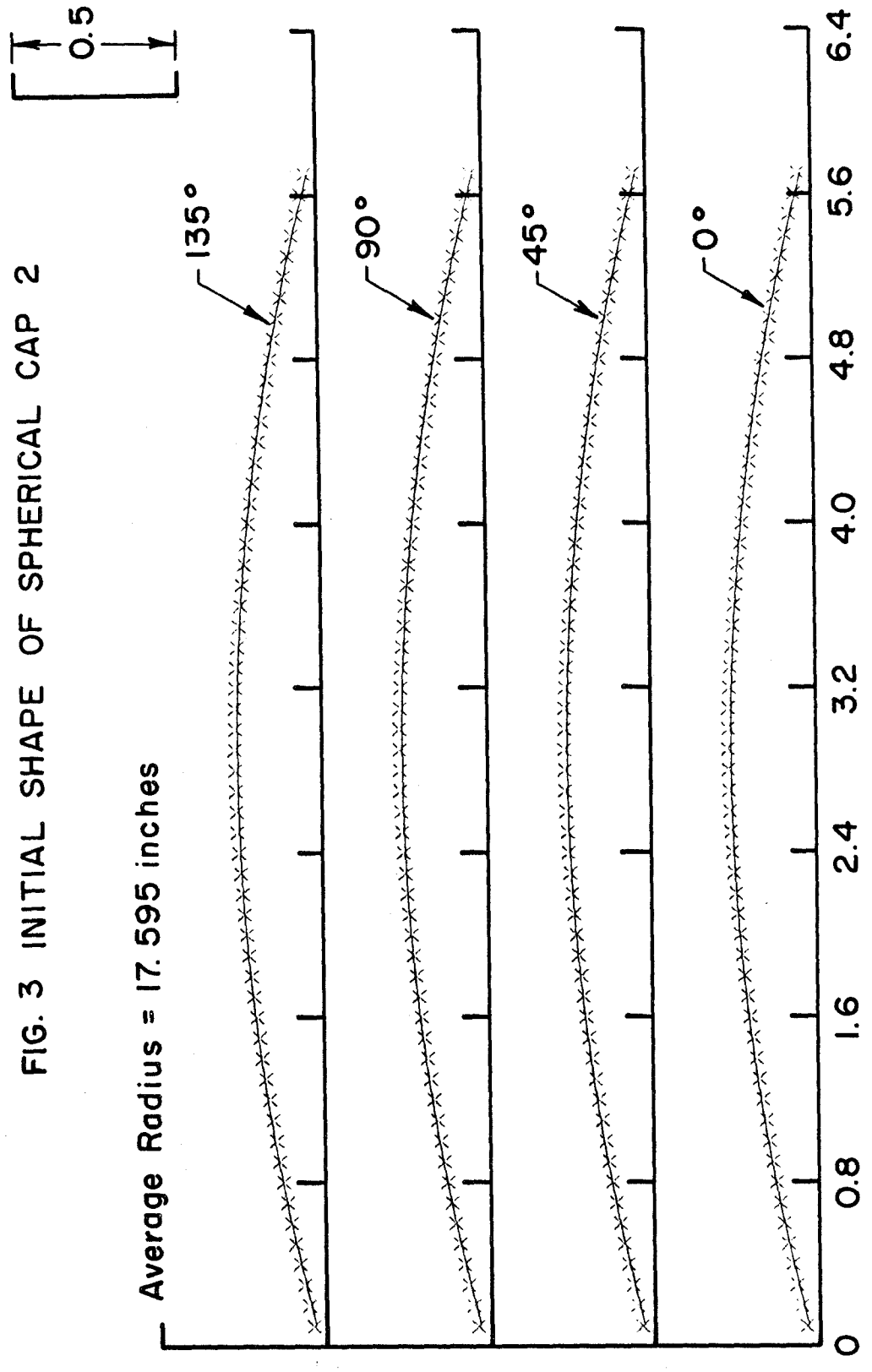

FIG. 3 INITIAL SHAPE OF SPHERICAL CAP 2

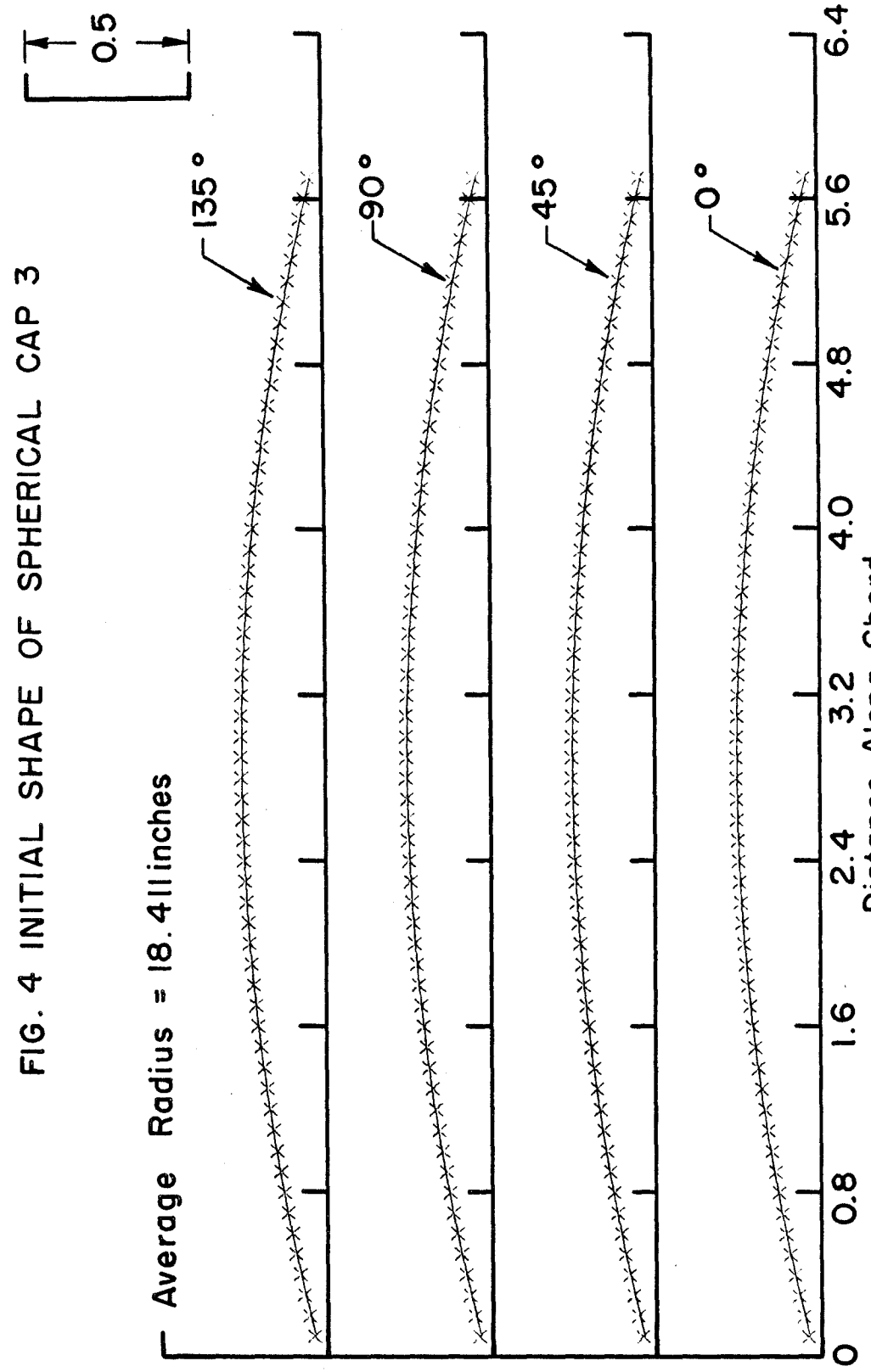

FIG. 4 INITIAL SHAPE OF SPHERICAL CAP 3

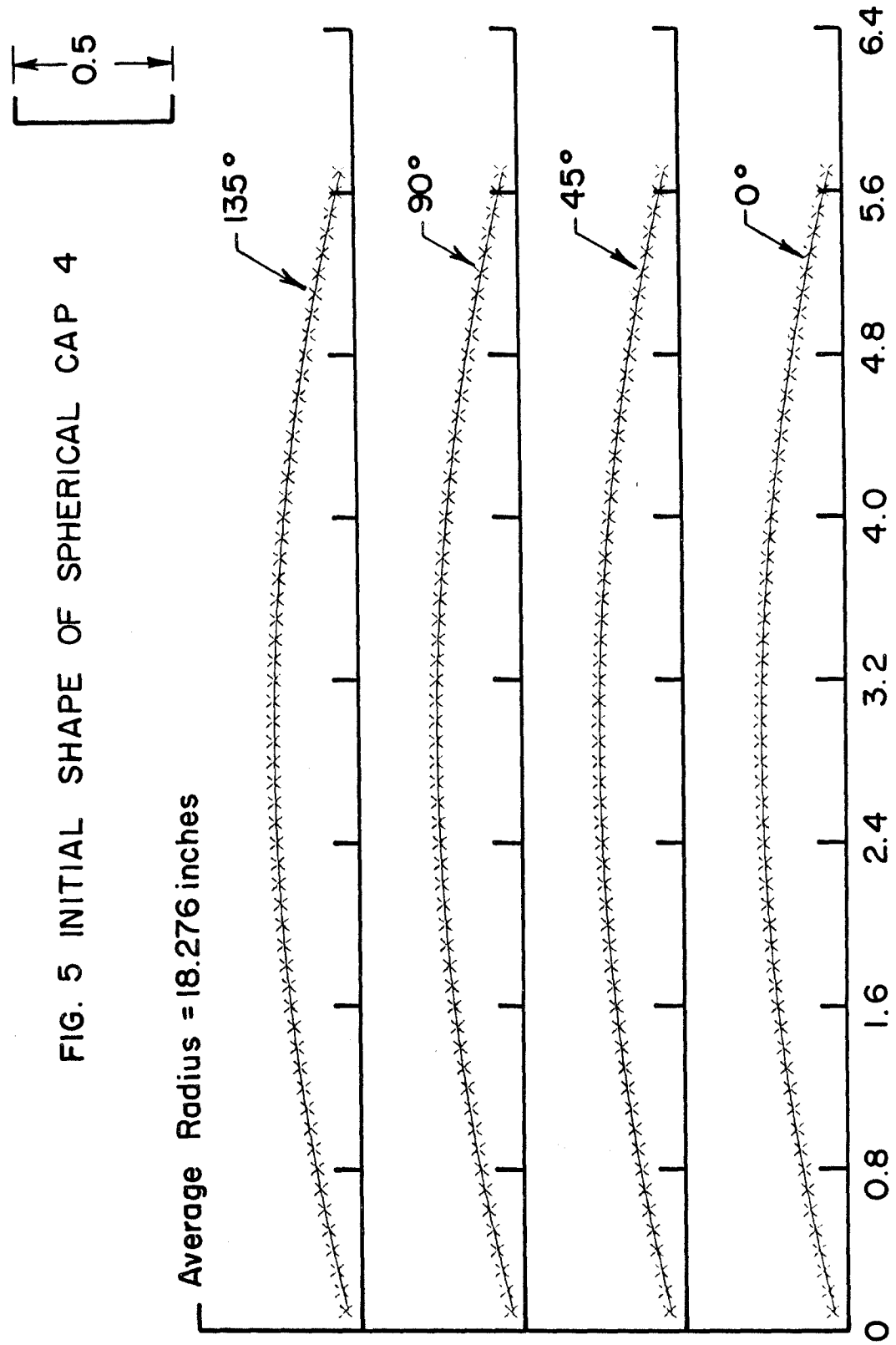

FIG. 5 INITIAL SHAPE OF SPHERICAL CAP 4

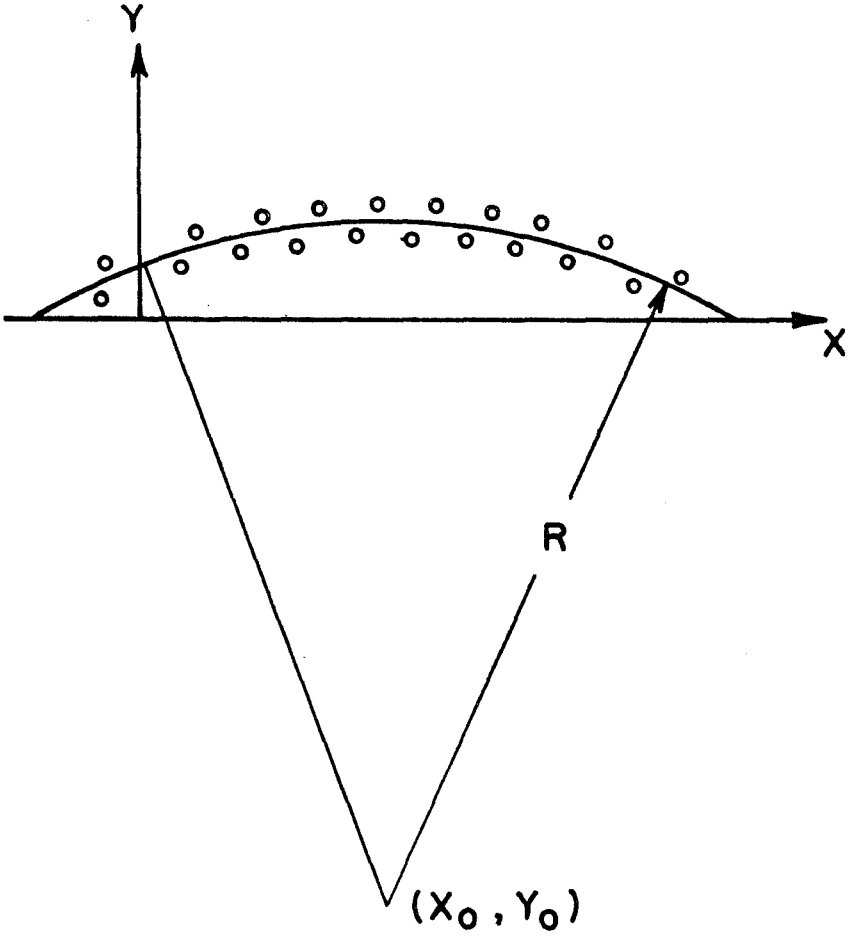

FIG. 6 COORDINATE SYSTEM FOR FINDING SPHERICAL CAP RADIUS

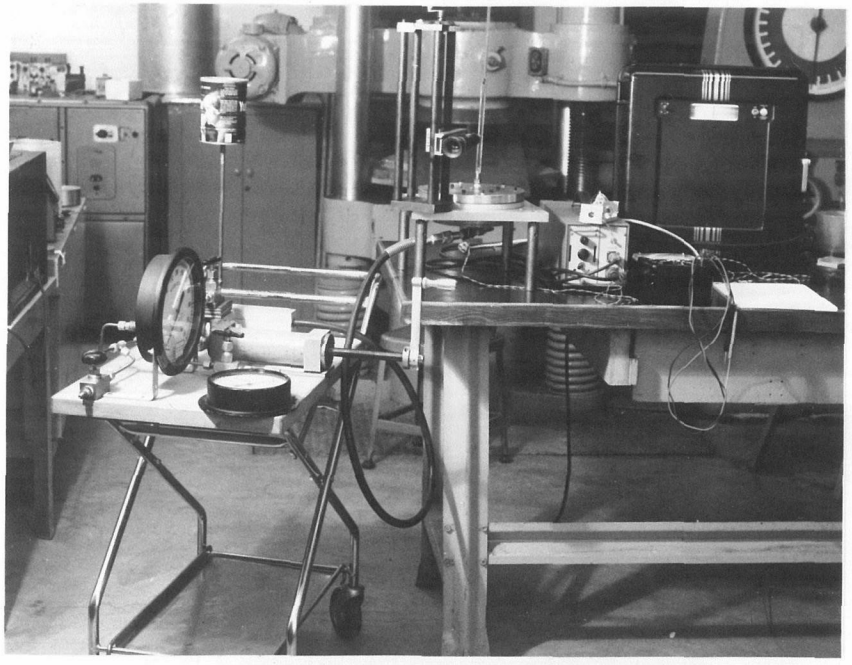

FIG. 7 EQUIPMENT USED IN STATIC TEST

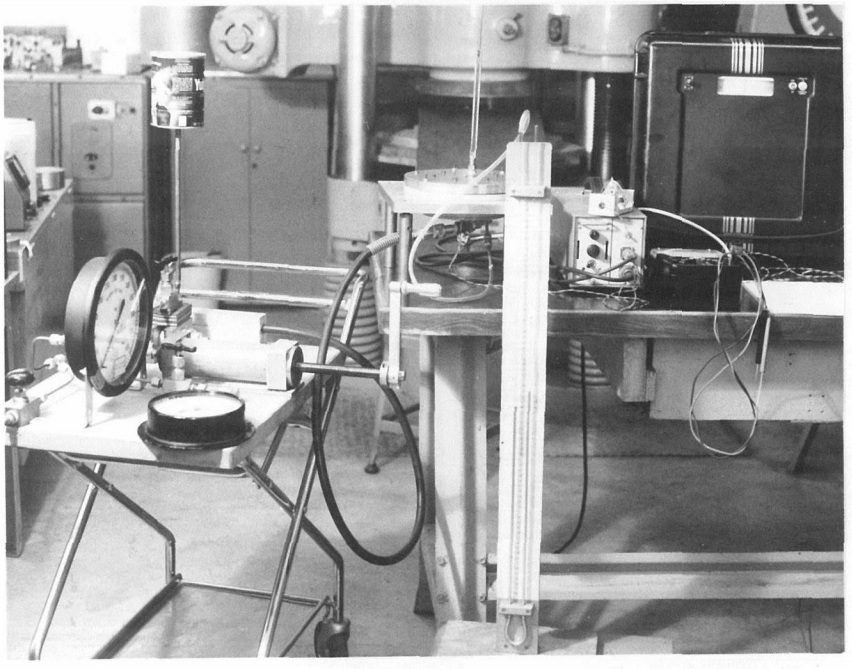

FIG. 8 EQUIPMENT USED IN PRESSURE CALIBRATION

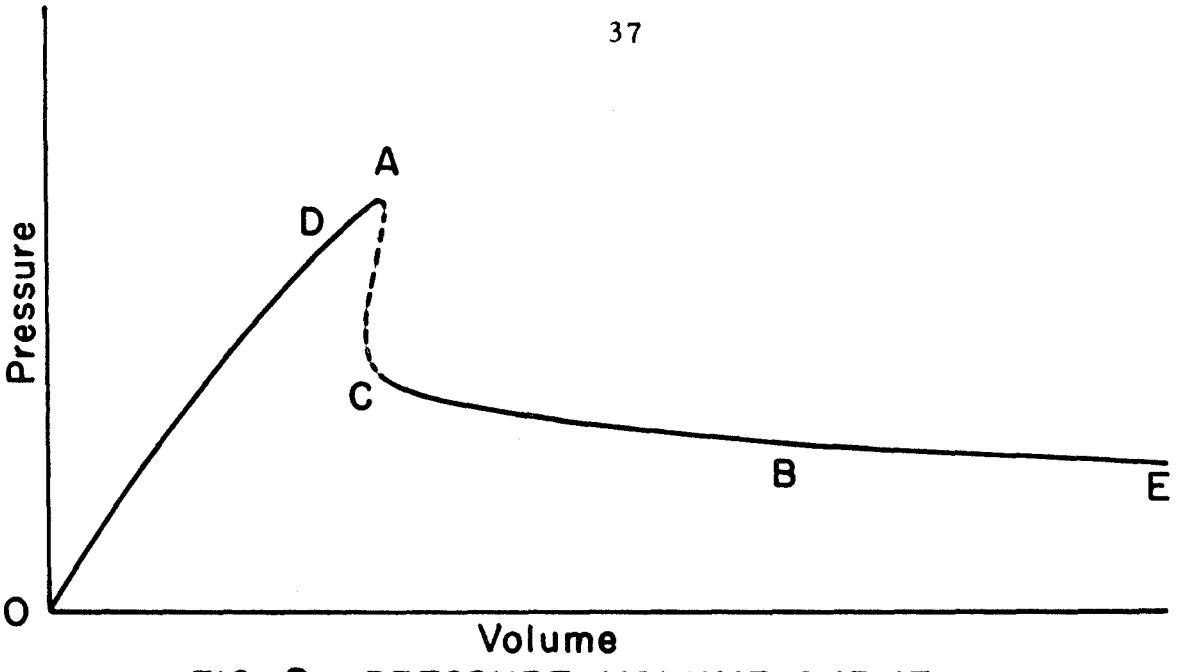

FIG. 9 PRESSURE VOLUME CURVE

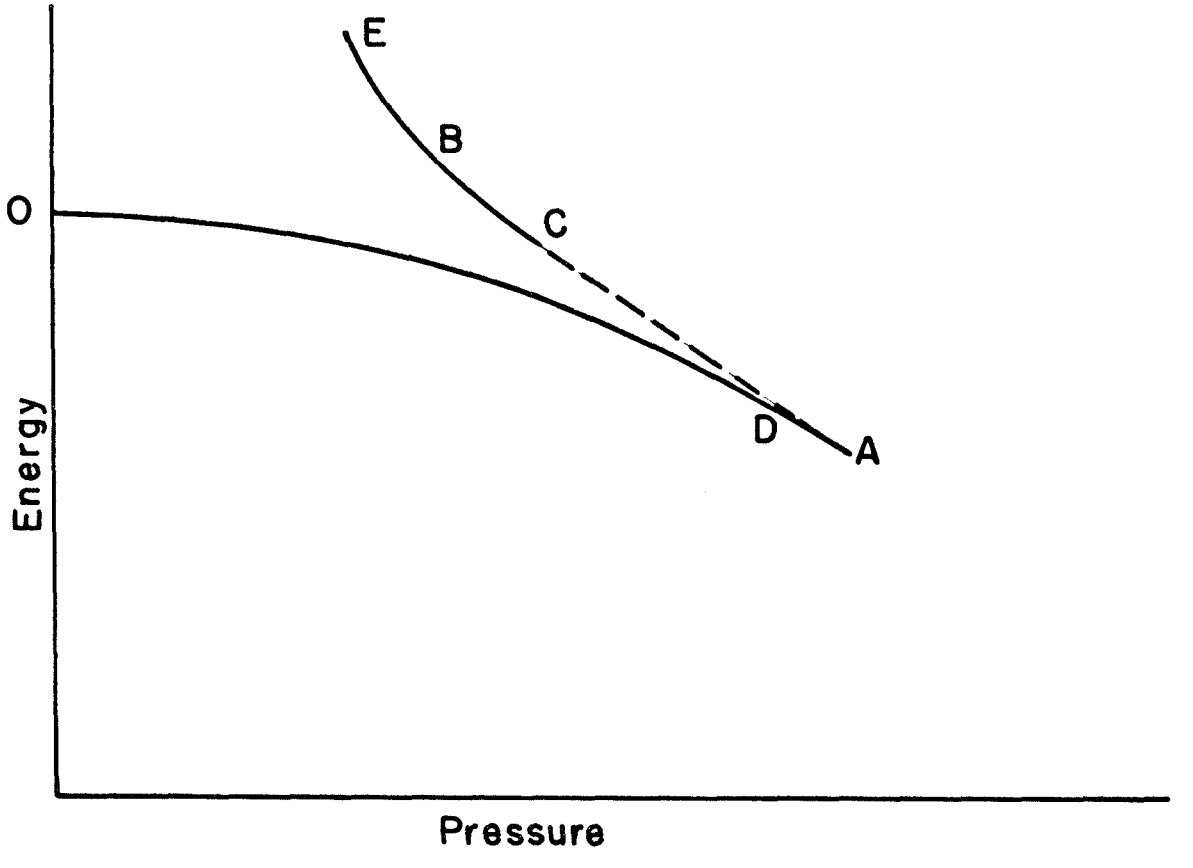

FIG. 10 POTENTIAL ENERGY VS. PRESSURE

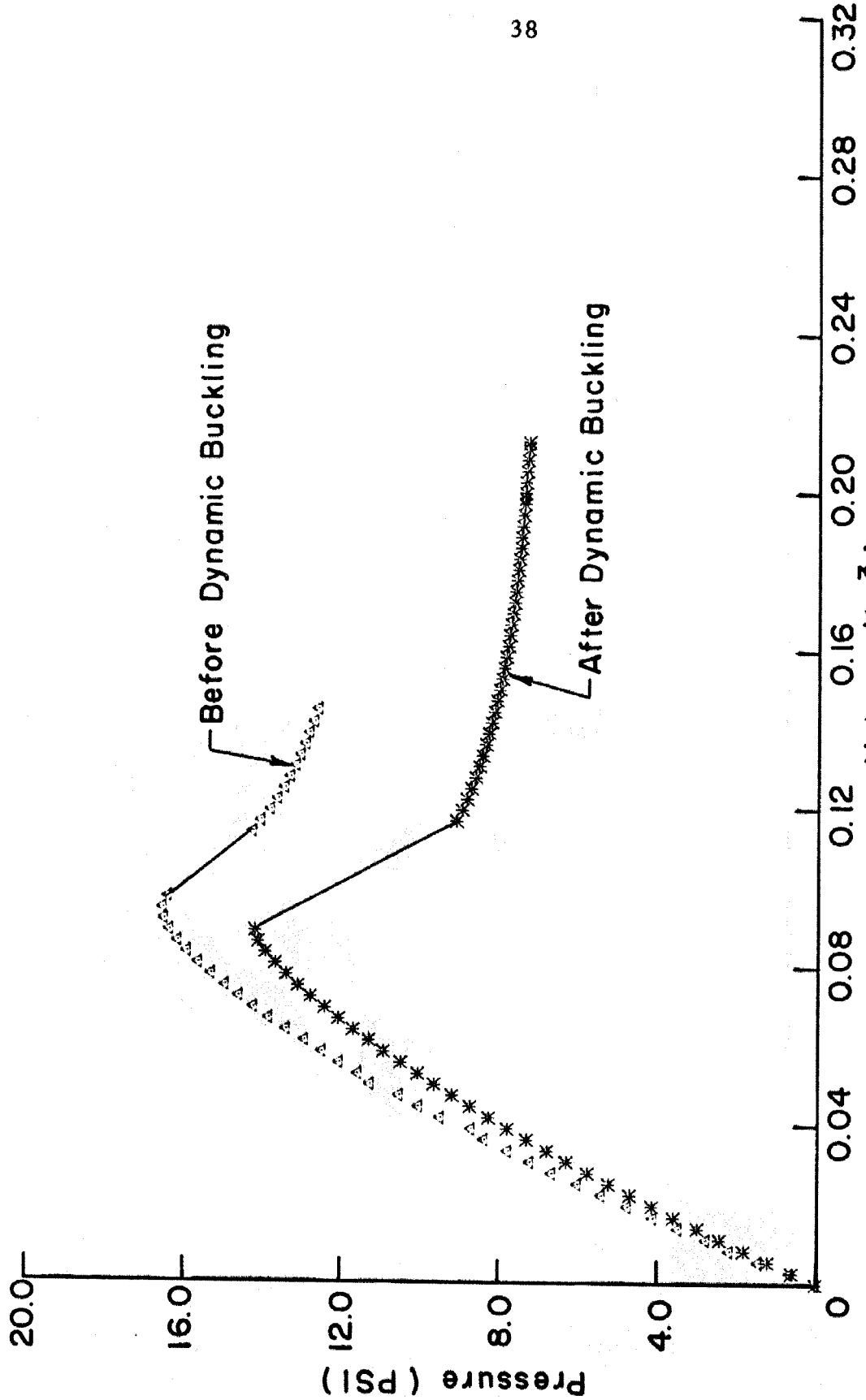

FIG.11 EXPERIMENTAL PRESSURE VOLUME CURVE FOR SPHERICAL CAP I

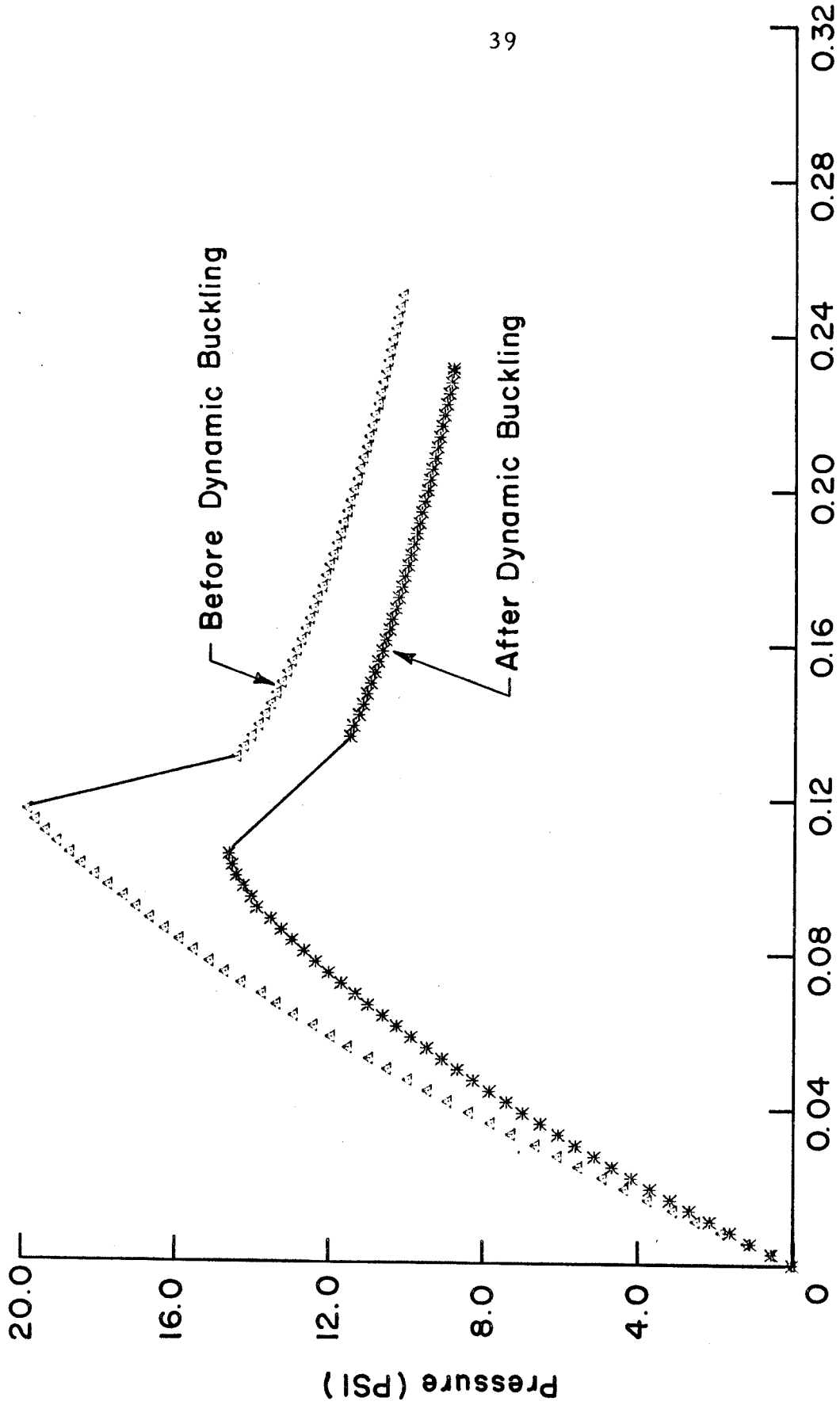

FIG. 12 EXPERIMENTAL PRESSURE VOLUME CURVE FOR SPHERICAL CAP 2

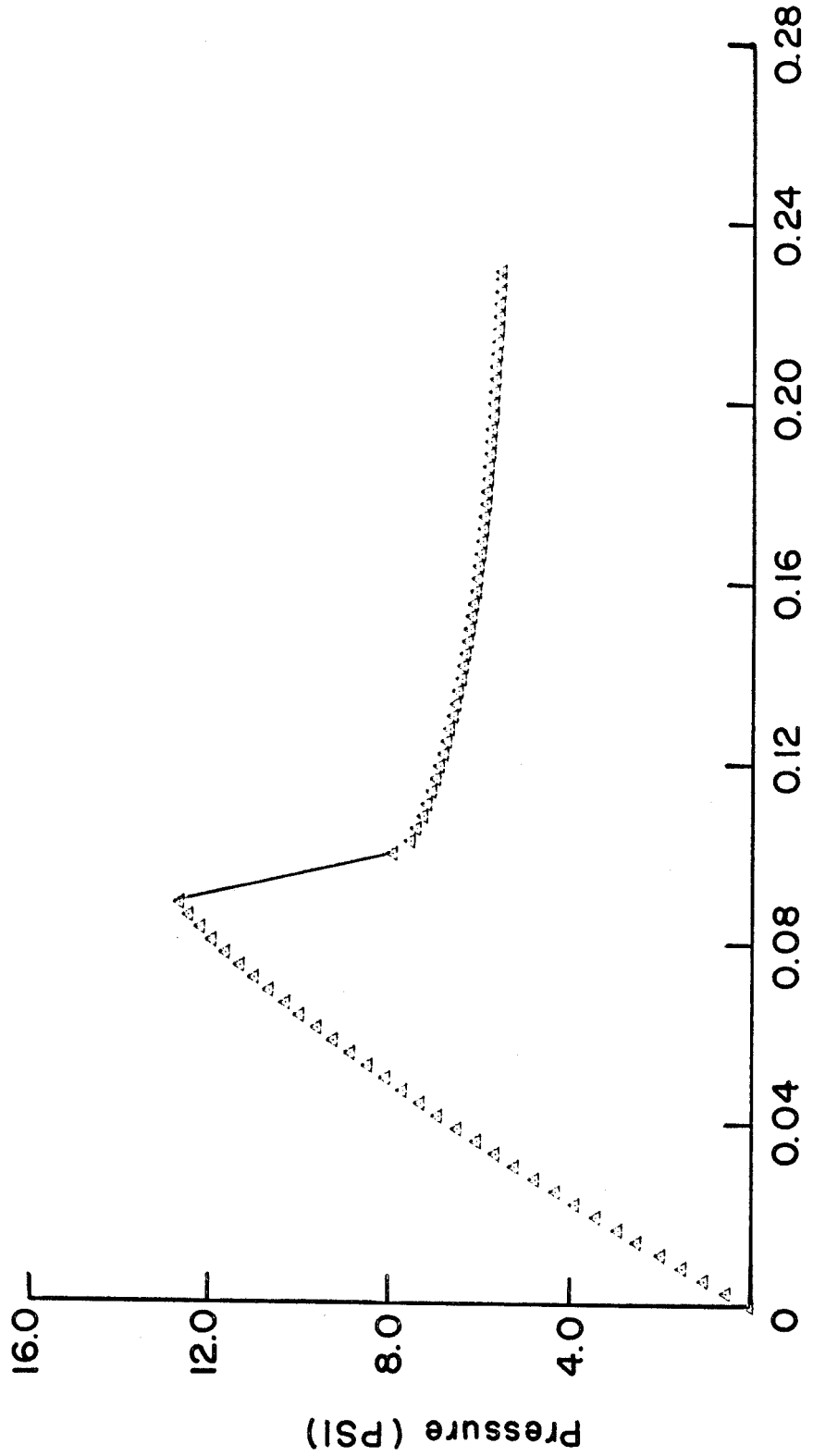

FIG. 13 EXPERIMENTAL PRESSURE VOLUME CURVE FOR SPHERICAL CAP 3 BEFORE DYNAMIC BUCKLING

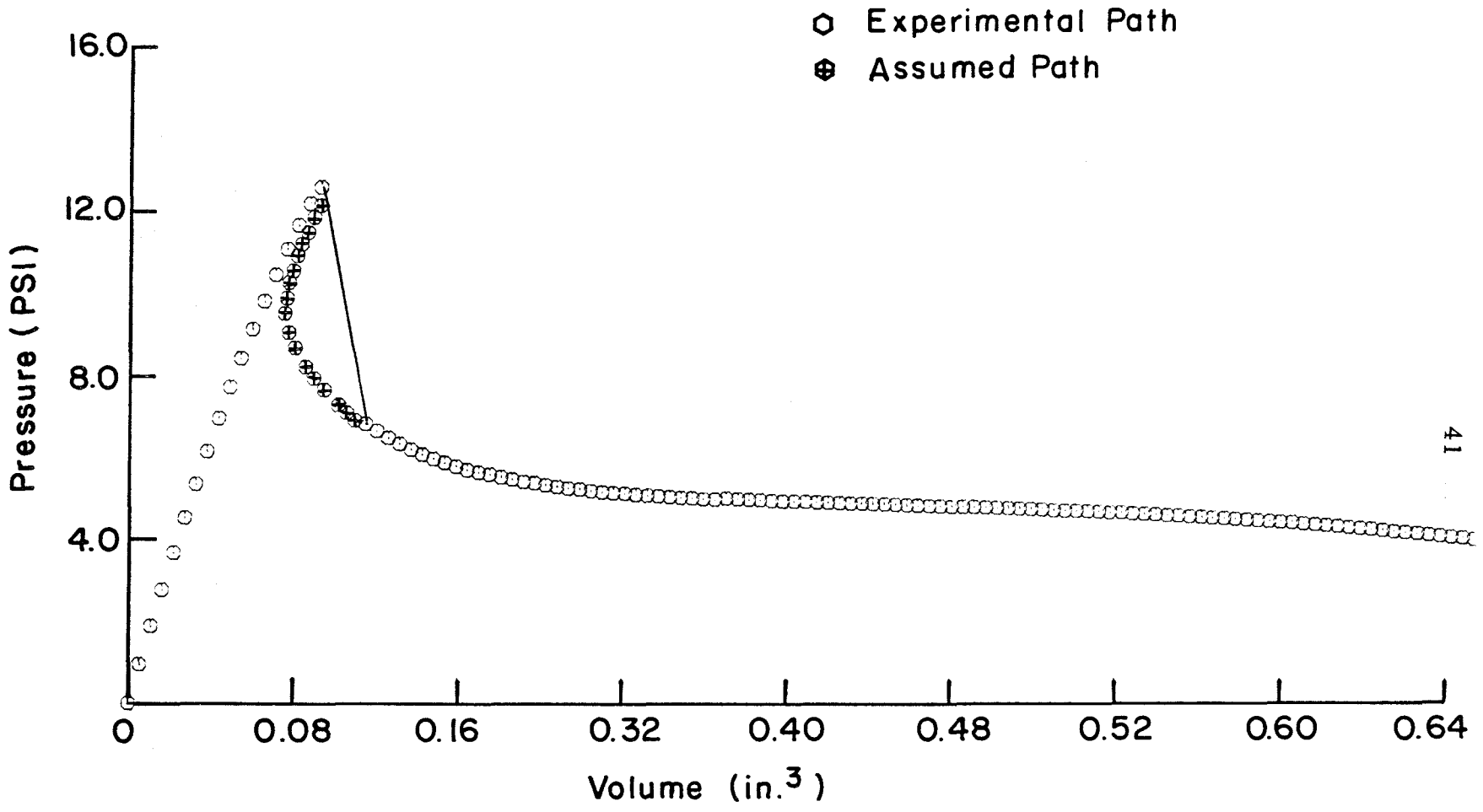

FIG. 14 EXPERIMENTAL PRESSURE VOLUME CURVE FOR SPHERICAL CAP 3 AFTER DYNAMIC BUCKLING. APPROXIMATED BY SPECIAL CURVE

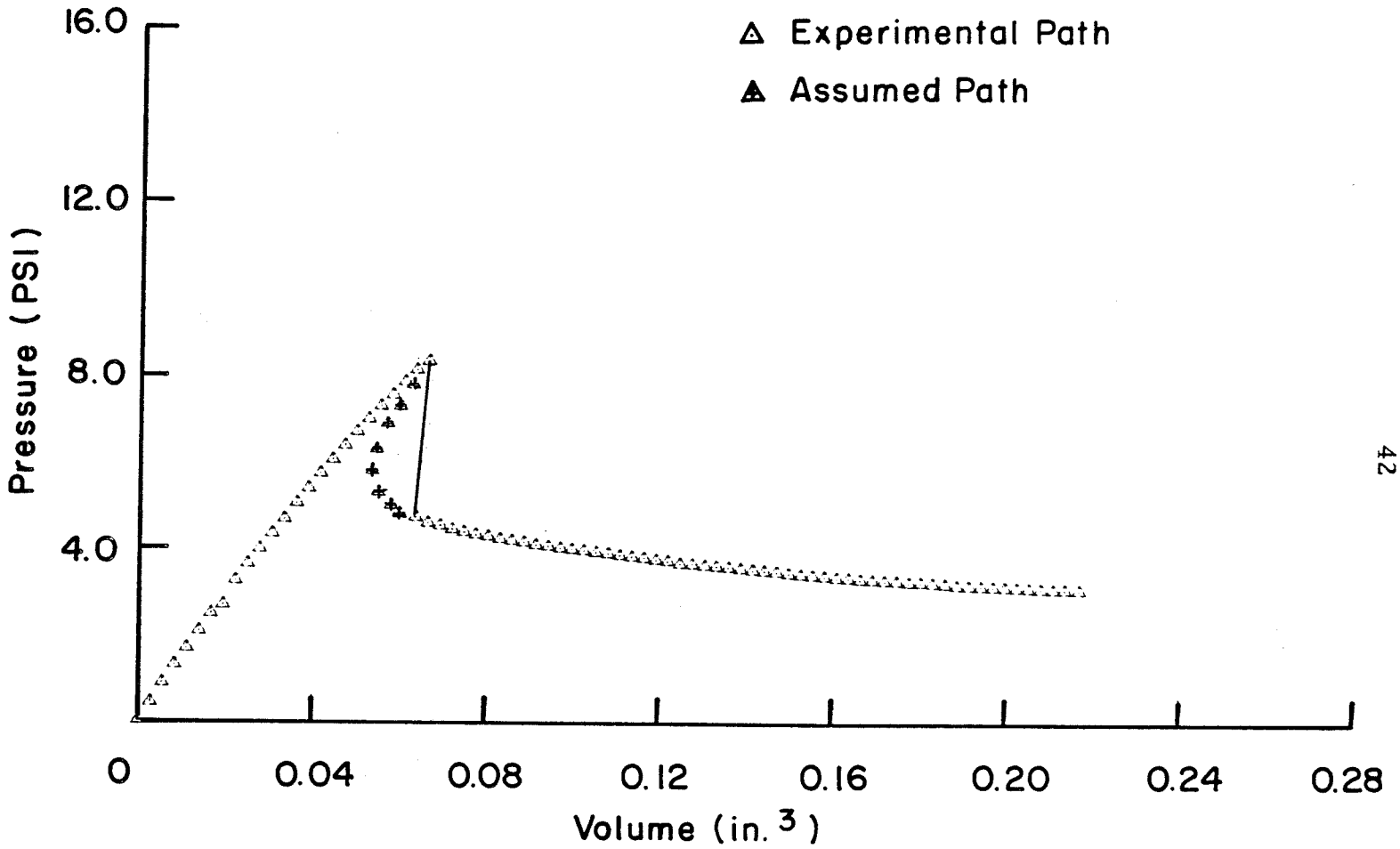

FIG. 15 EXPERIMENTAL PRESSURE VOLUME CURVE FOR SPHERICAL CAP 4 BEFORE DYNAMIC BUCKLING. APPROXIMATED BY SPECIAL CURVE

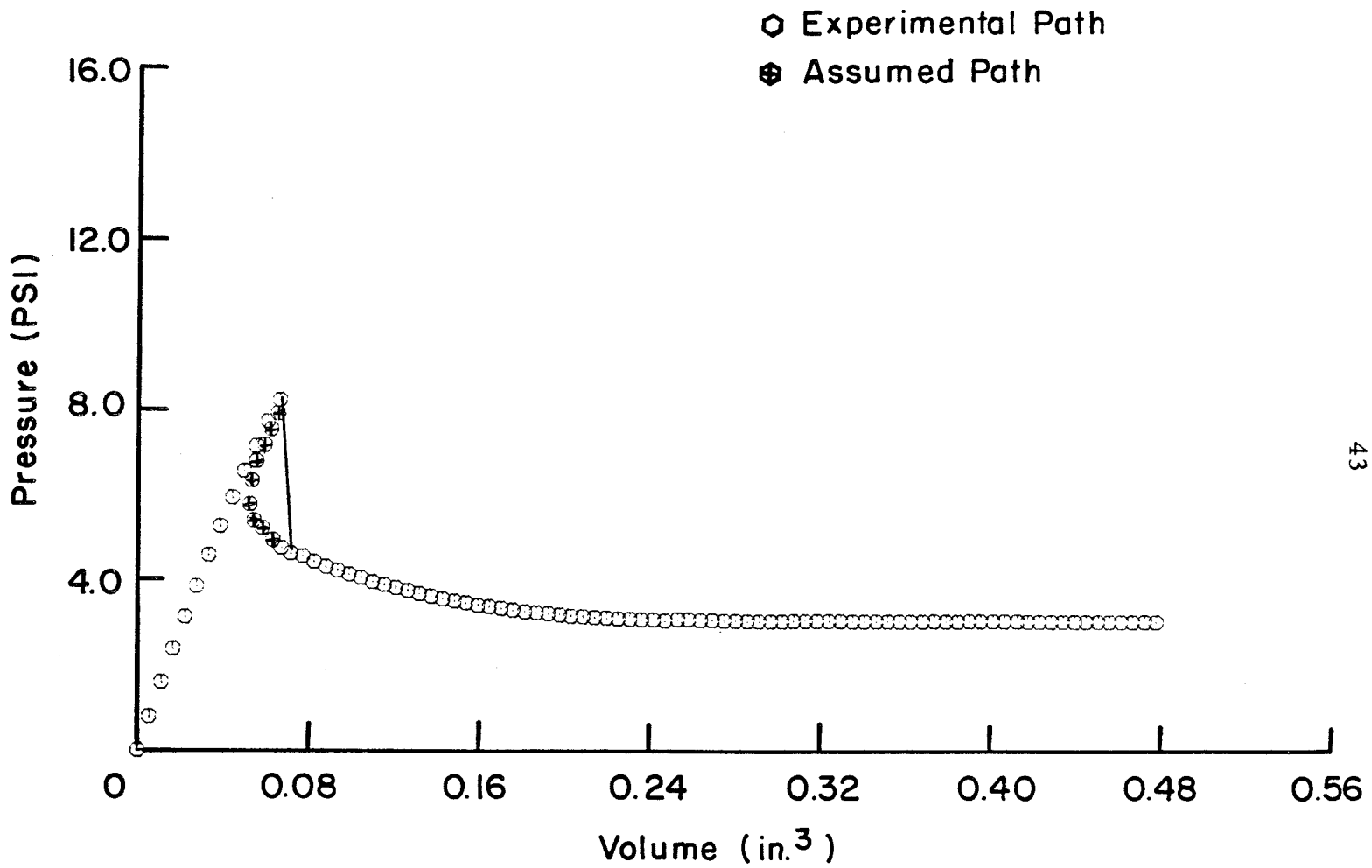

FIG. 16 EXPERIMENTAL PRESSURE VOLUME CURVE FOR SPHERICAL CAP 4 AFTER DYNAMIC BUCKLING. APPROXIMATED BY SPECIAL CURVE

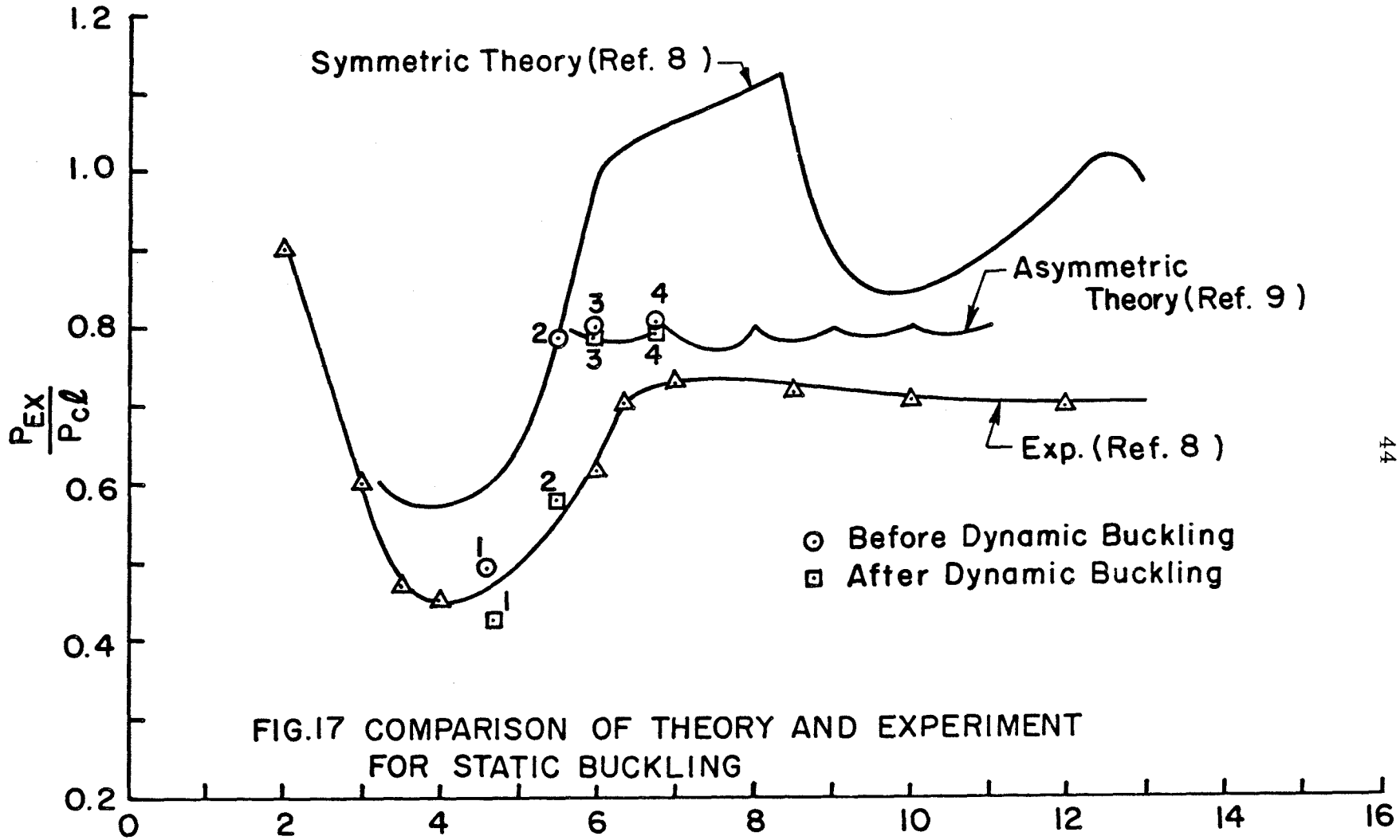

FIG.17 COMPARISON OF THEORY AND EXPERIMENT FOR STATIC BUCKLING

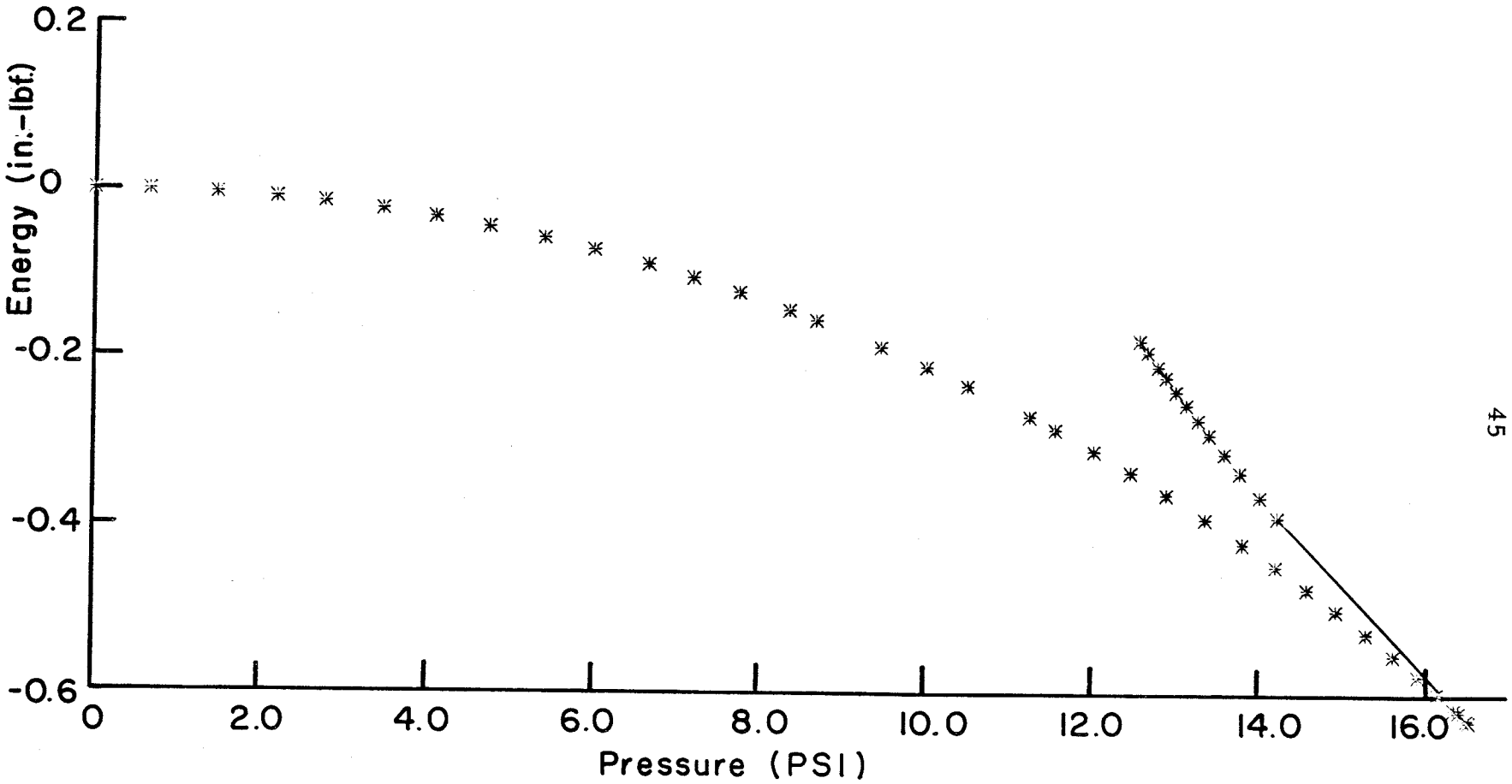

FIG. 18 POTENTIAL ENERGY VS. PRESSURE FOR SPHERICAL CAP I BEFORE DYNAMIC BUCKLING

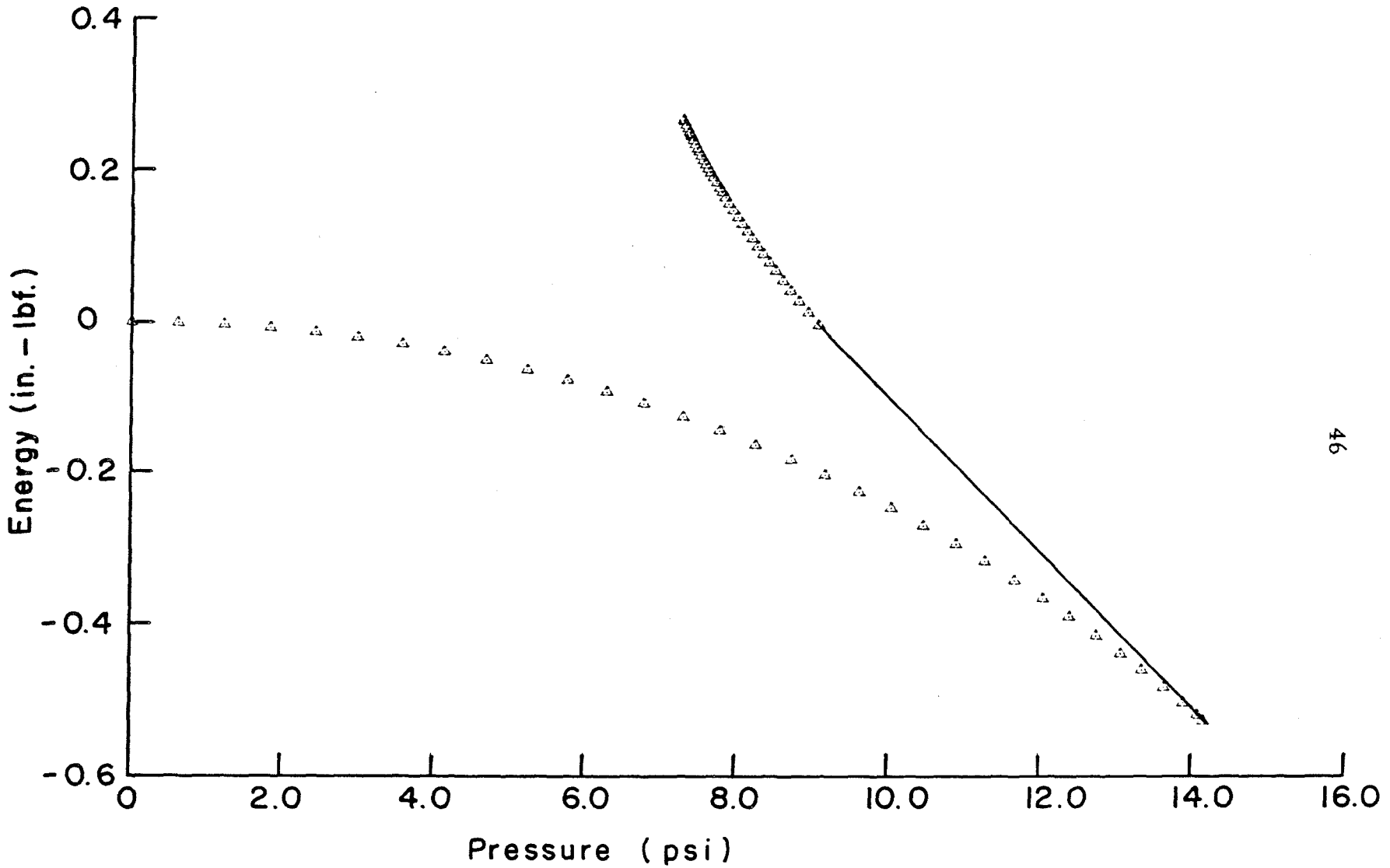

FIG.19 POTENTIAL ENERGY VS. PRESSURE FOR SPHERICAL CAP I AFTER DYNAMIC BUCKLING

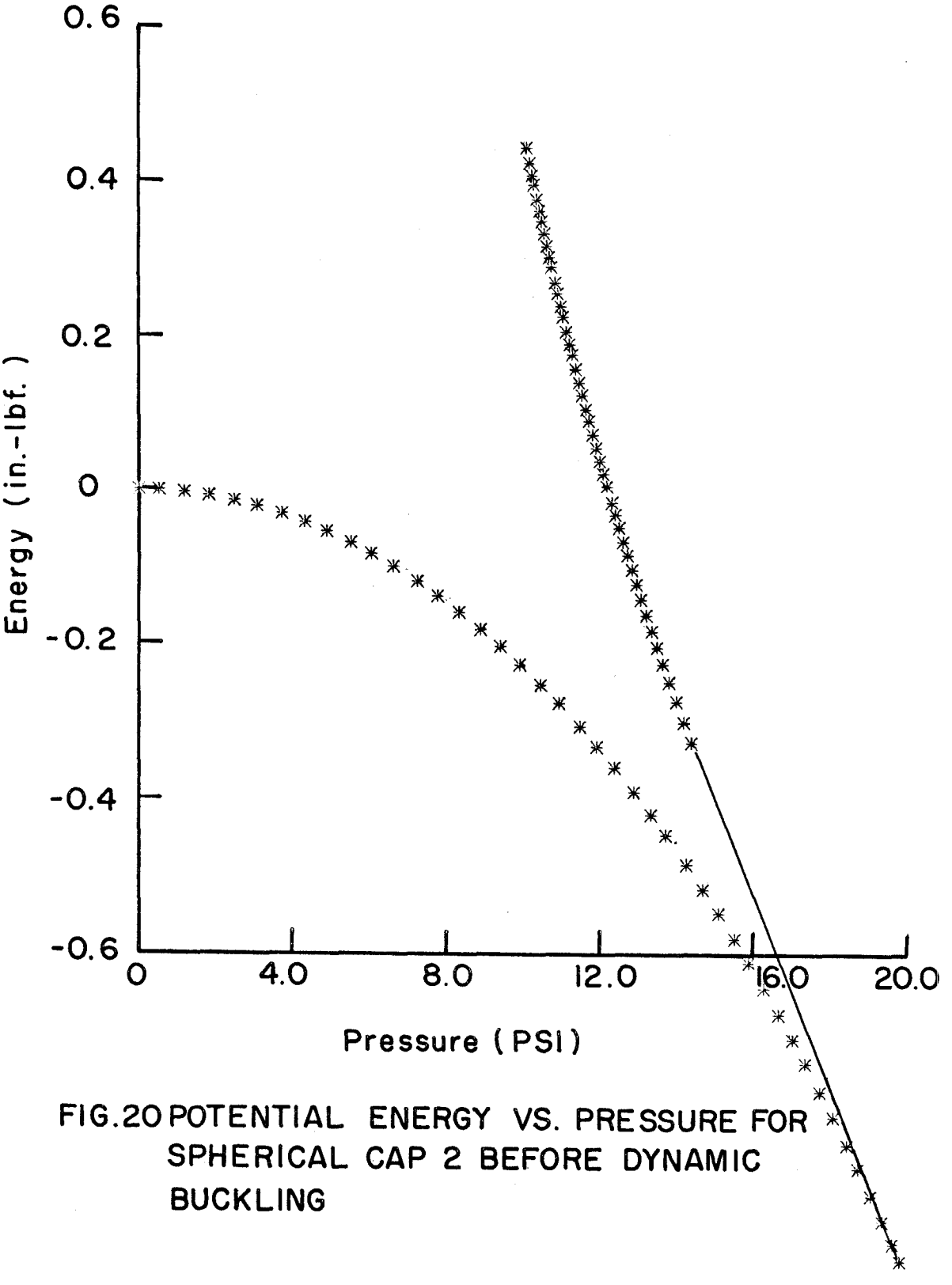

FIG. 20 POTENTIAL ENERGY VS. PRESSURE FOR SPHERICAL CAP 2 BEFORE DYNAMIC BUCKLING

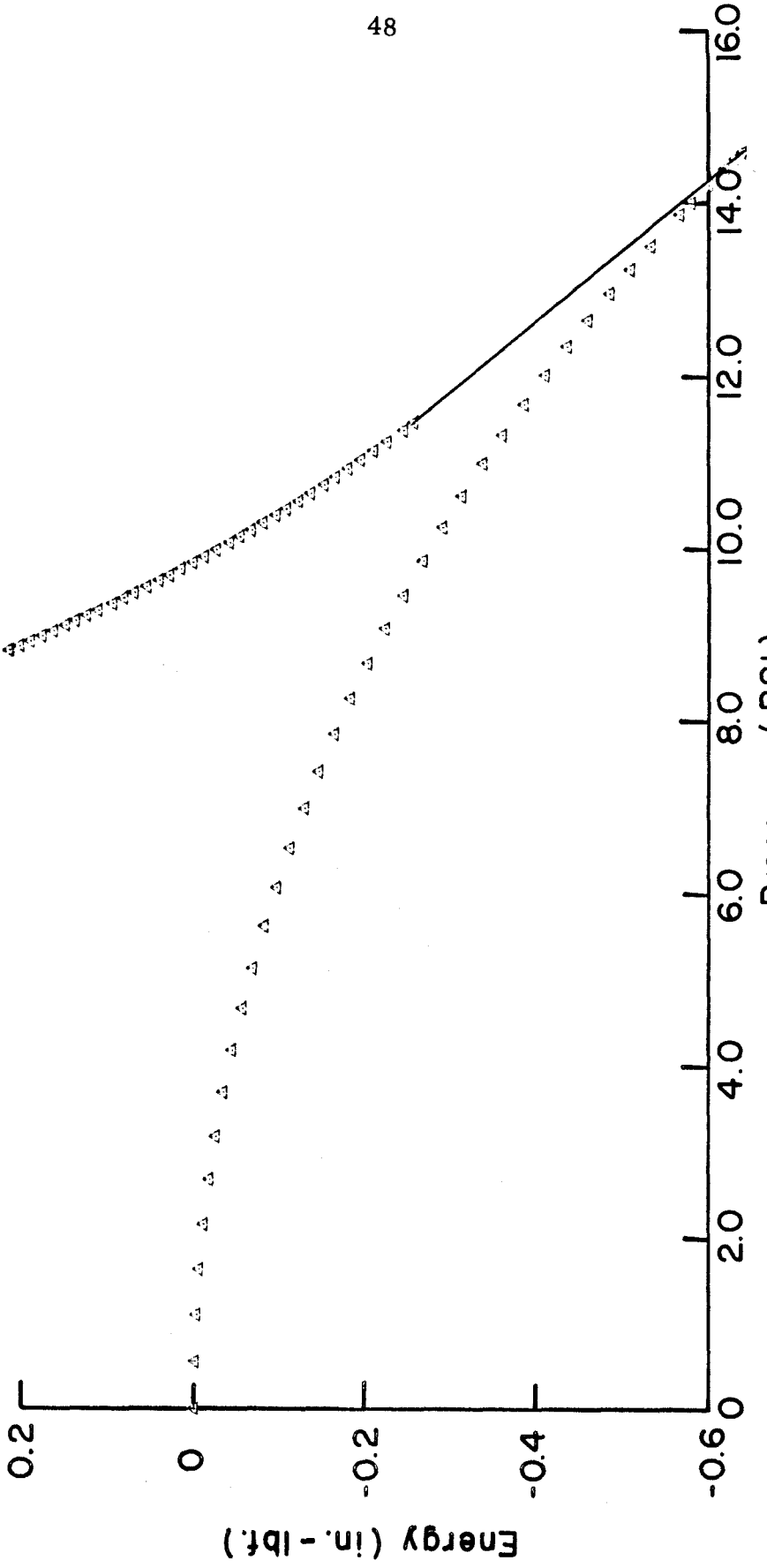

FIG. 21 POTENTIAL ENERGY VS. PRESSURE FOR SPHERICAL CAP 2 AFTER DYNAMIC BUCKLING

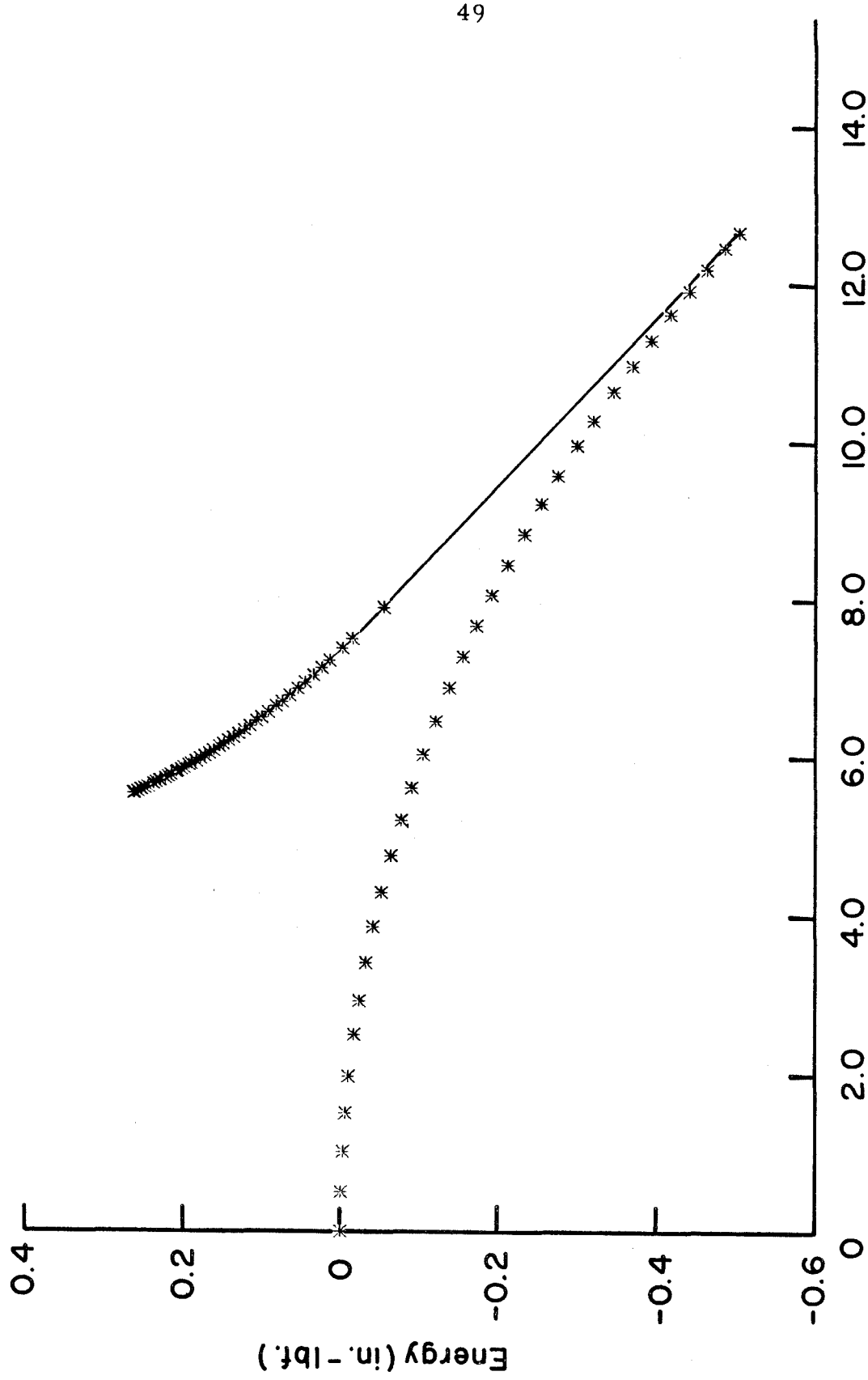

FIG.22 POTENTIAL ENERGY VS. PRESSURE FOR SPHERICAL CAP 3 BEFORE DYNAMIC BUCKLING

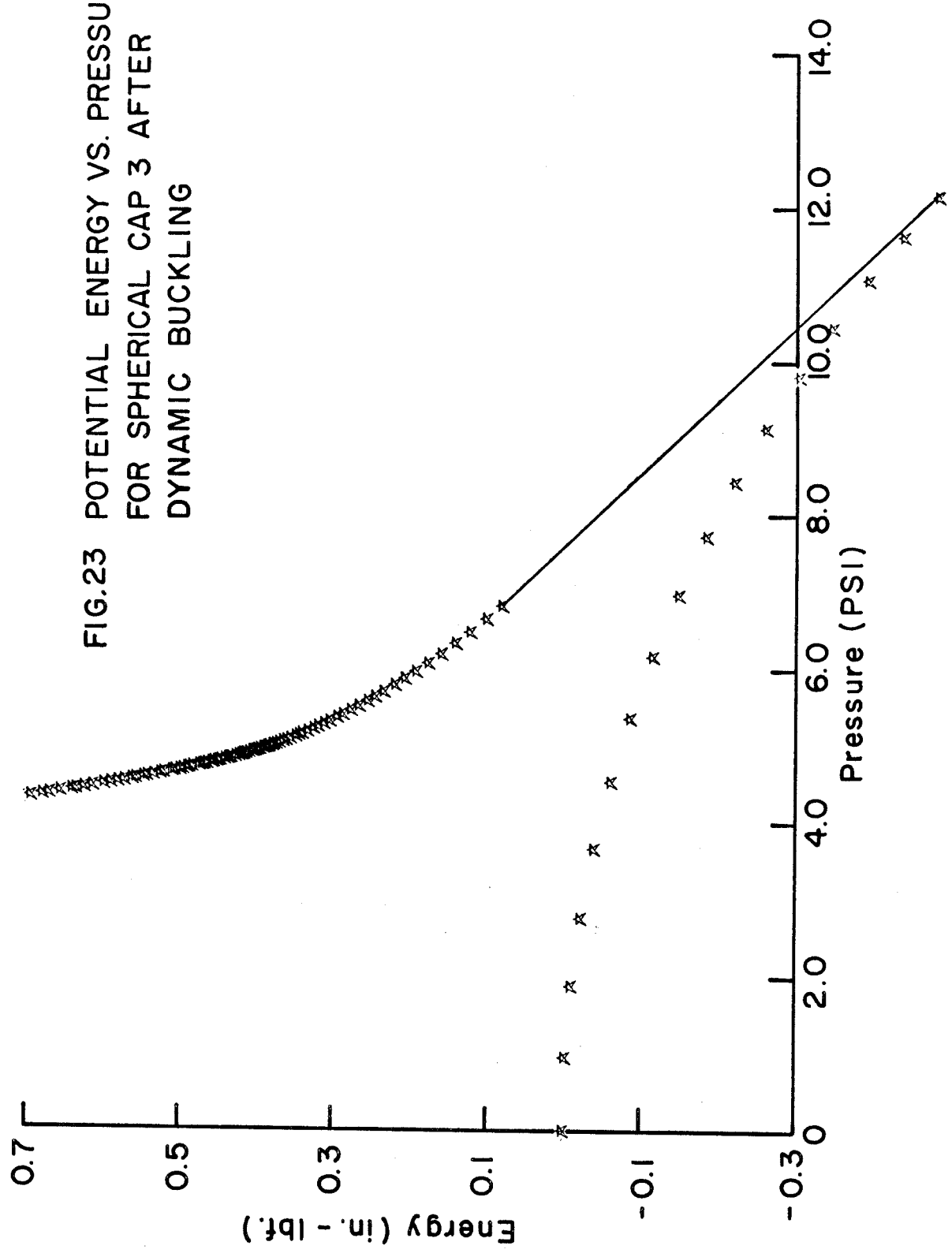

FIG.23 POTENTIAL ENERGY VS. PRESSURE FOR SPHERICAL CAP 3 AFTER DYNAMIC BUCKLING

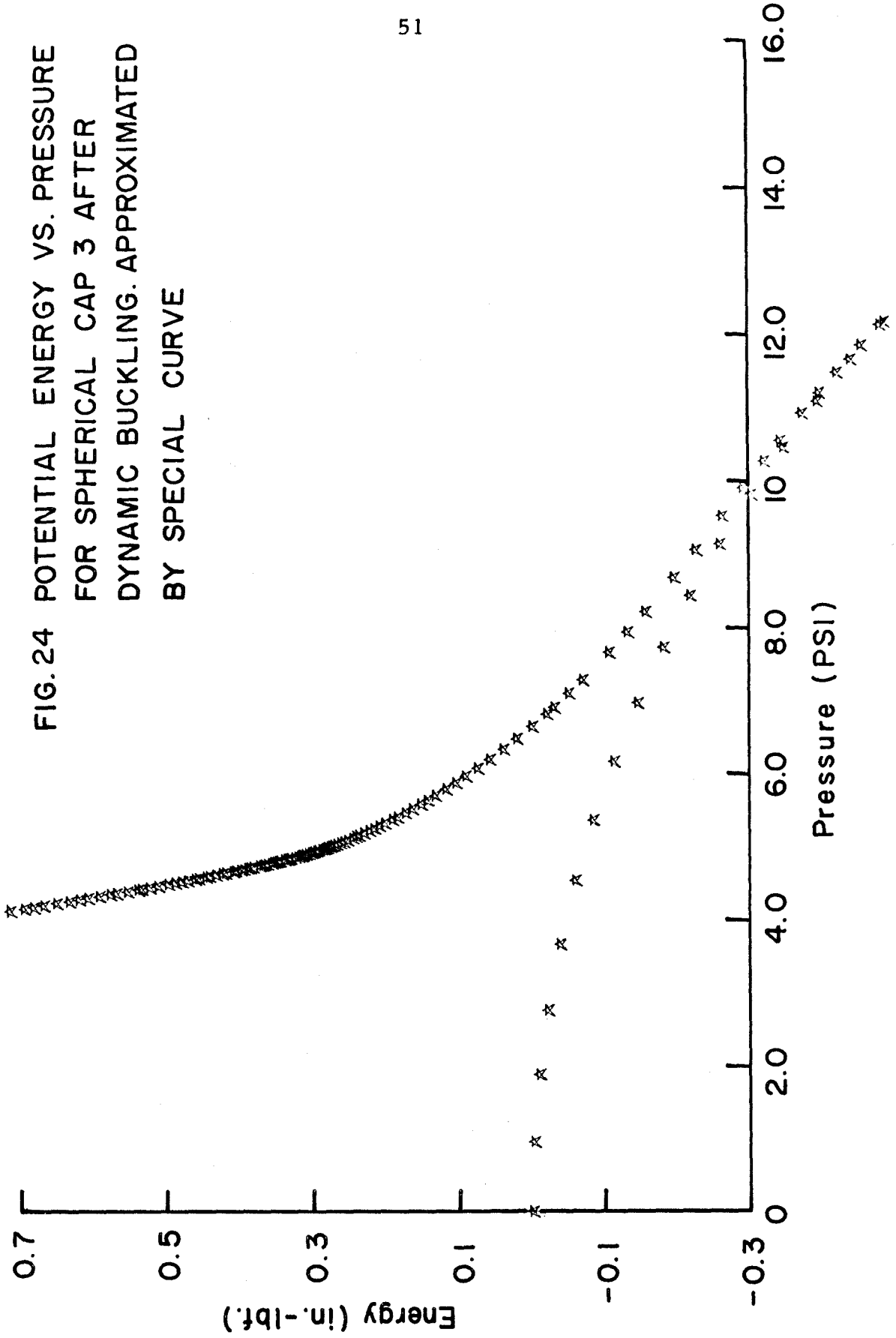

FIG. 24 POTENTIAL ENERGY VS. PRESSURE FOR SPHERICAL CAP 3 AFTER DYNAMIC BUCKLING. APPROXIMATED BY SPECIAL CURVE

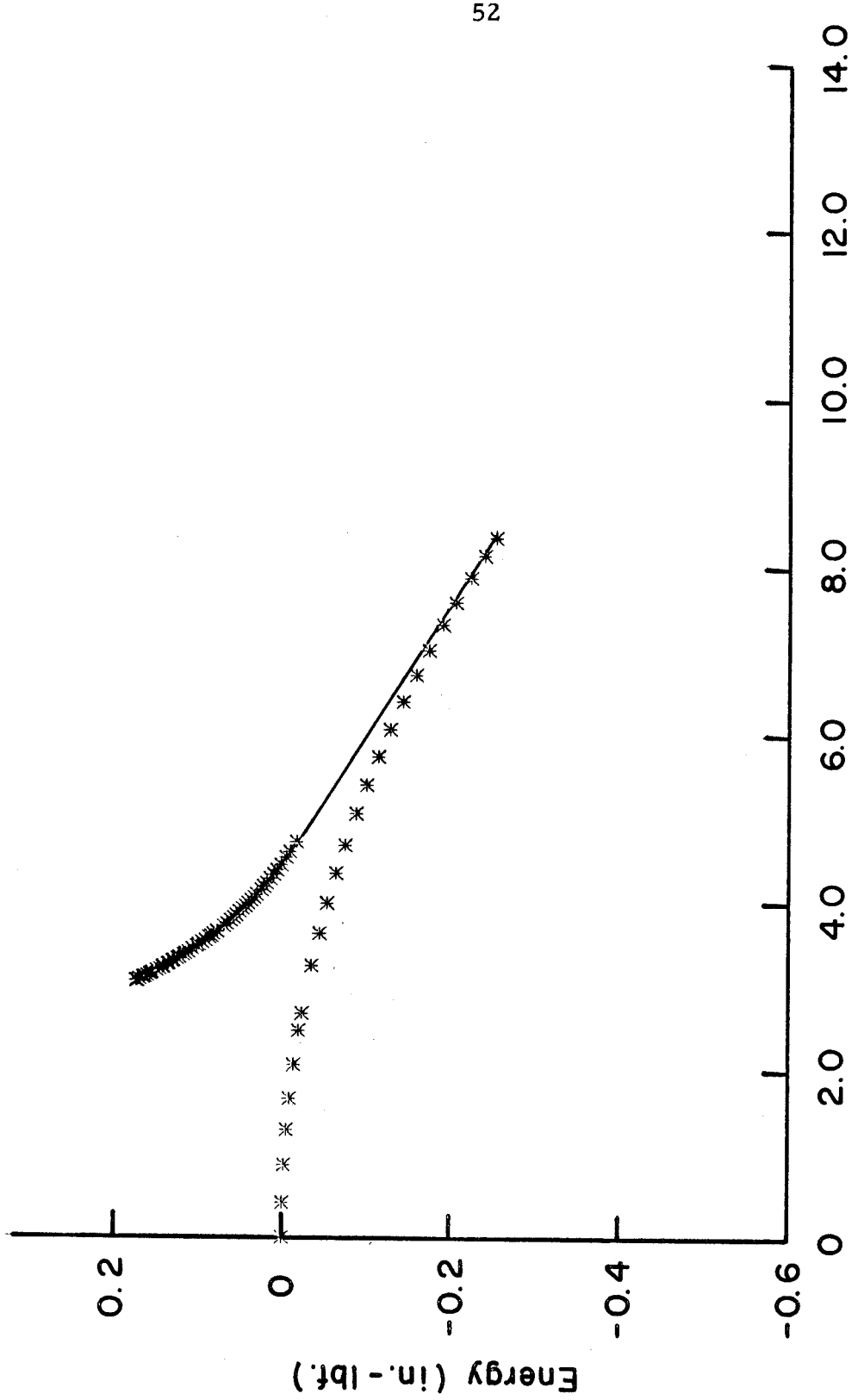

FIG. 25 POTENTIAL ENERGY VS. PRESSURE FOR SPHERICAL CAP 4
BEFORE DYNAMIC BUCKLING

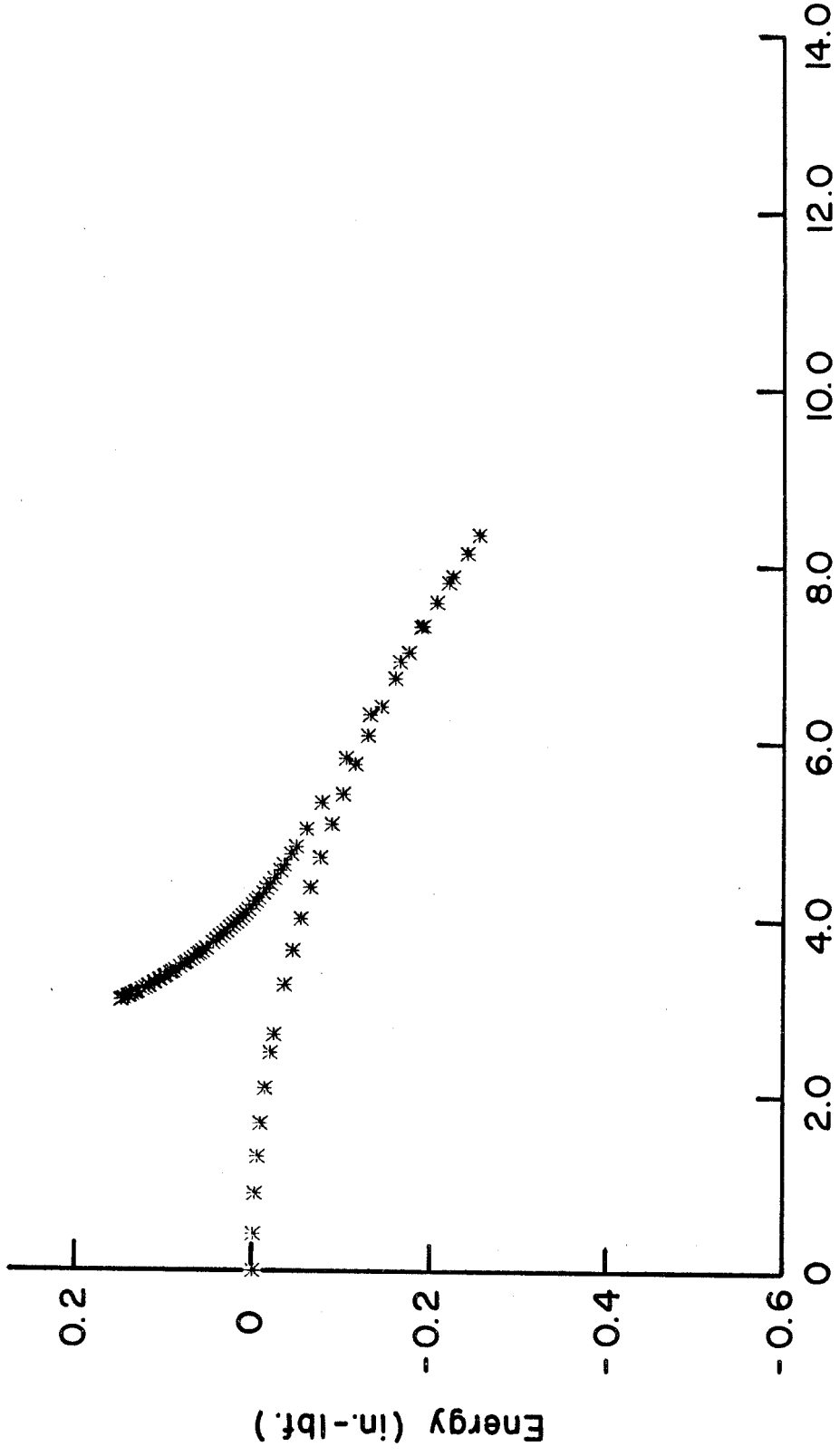

FIG. 26 POTENTIAL ENERGY VS. PRESSURE FOR SPHERICAL CAP 4 BEFORE DYNAMIC BUCKLING. APPROXIMATED BY SPECIAL CURVE

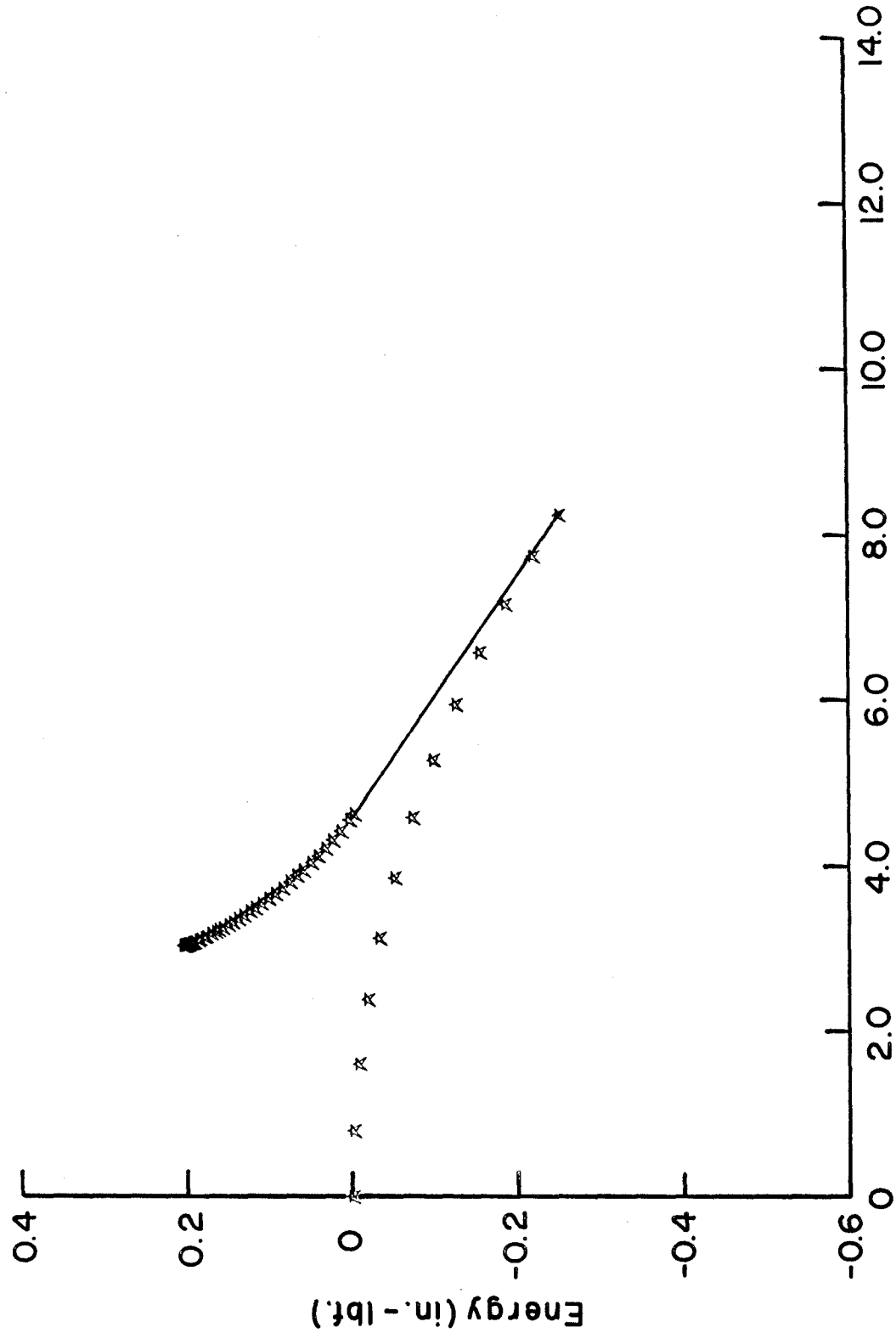

FIG.27 POTENTIAL ENERGY VS. PRESSURE FOR SPHERICAL CAP 4 AFTER DYNAMIC BUCKLING

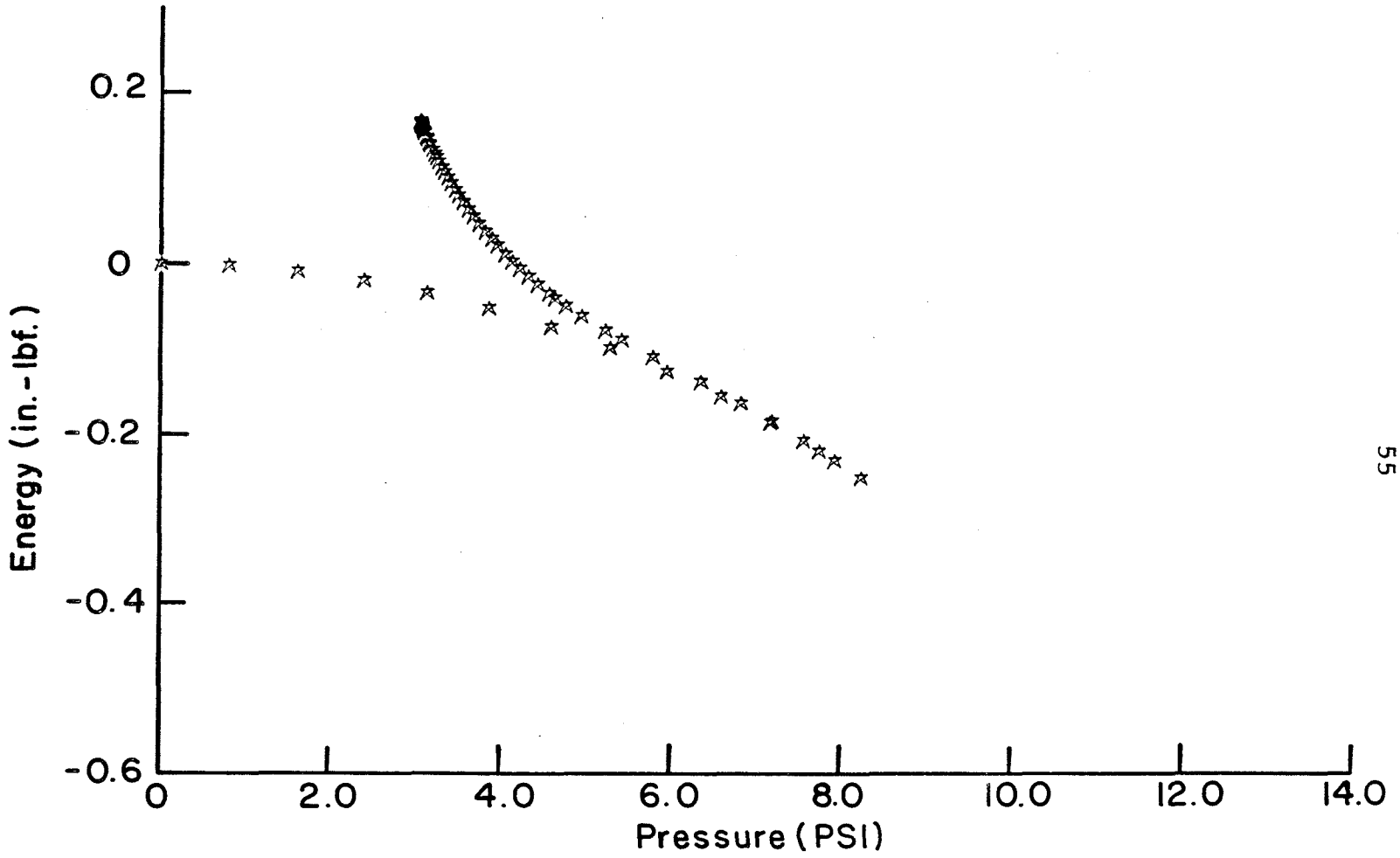

FIG. 28 POTENTIAL ENERGY VS. PRESSURE FOR SPHERICAL CAP 4 AFTER DYNAMIC BUCKLING. APPROXIMATED BY SPECIAL CURVE

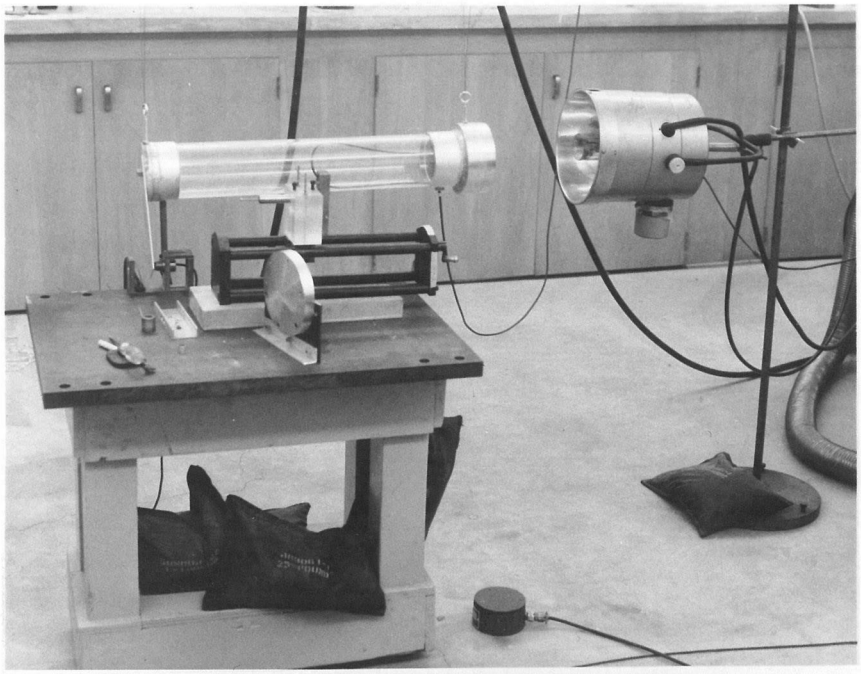

FIG. 29 PENDULUM

FIG. 30 EQUIPMENT USED IN THE DYNAMIC TEST

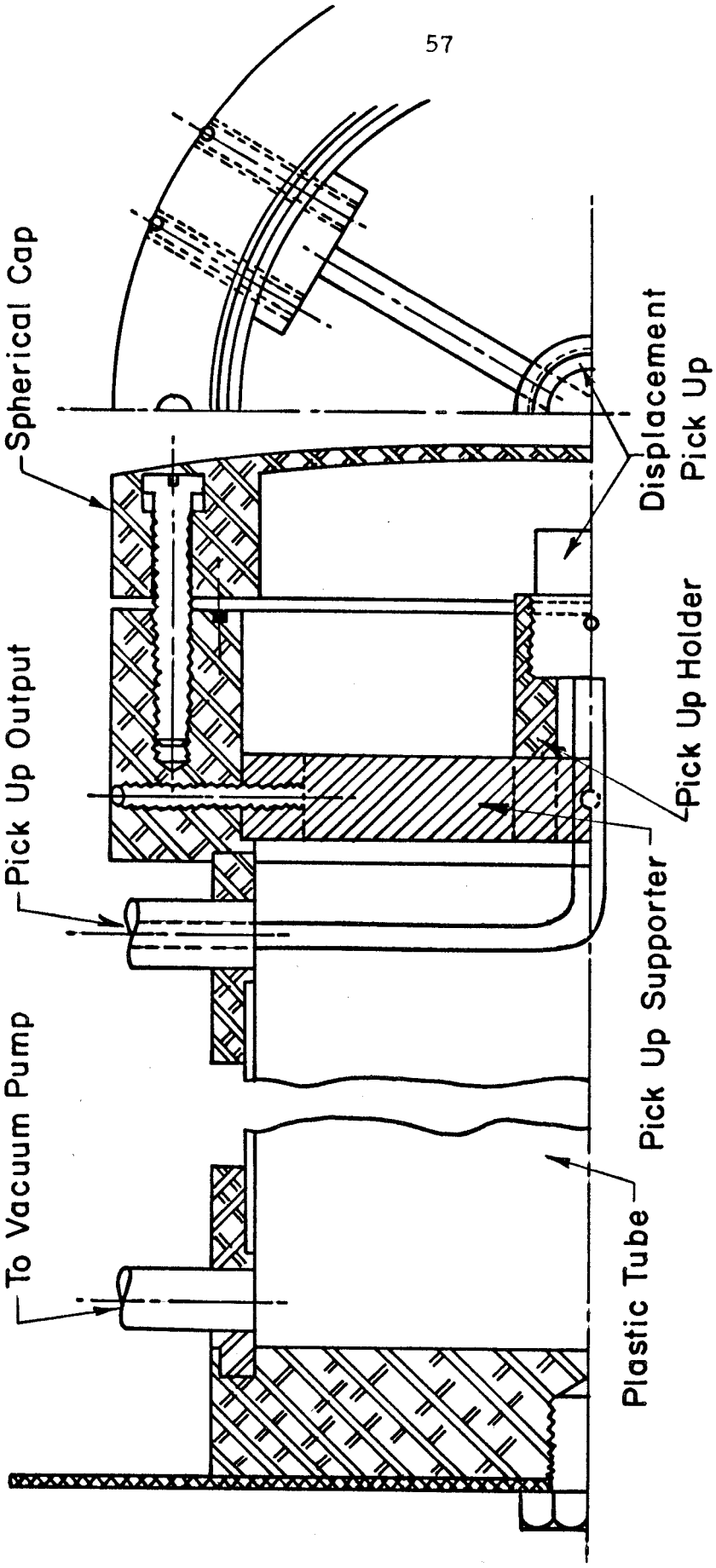

FIG. 31 DYNAMIC TEST APPARATUS

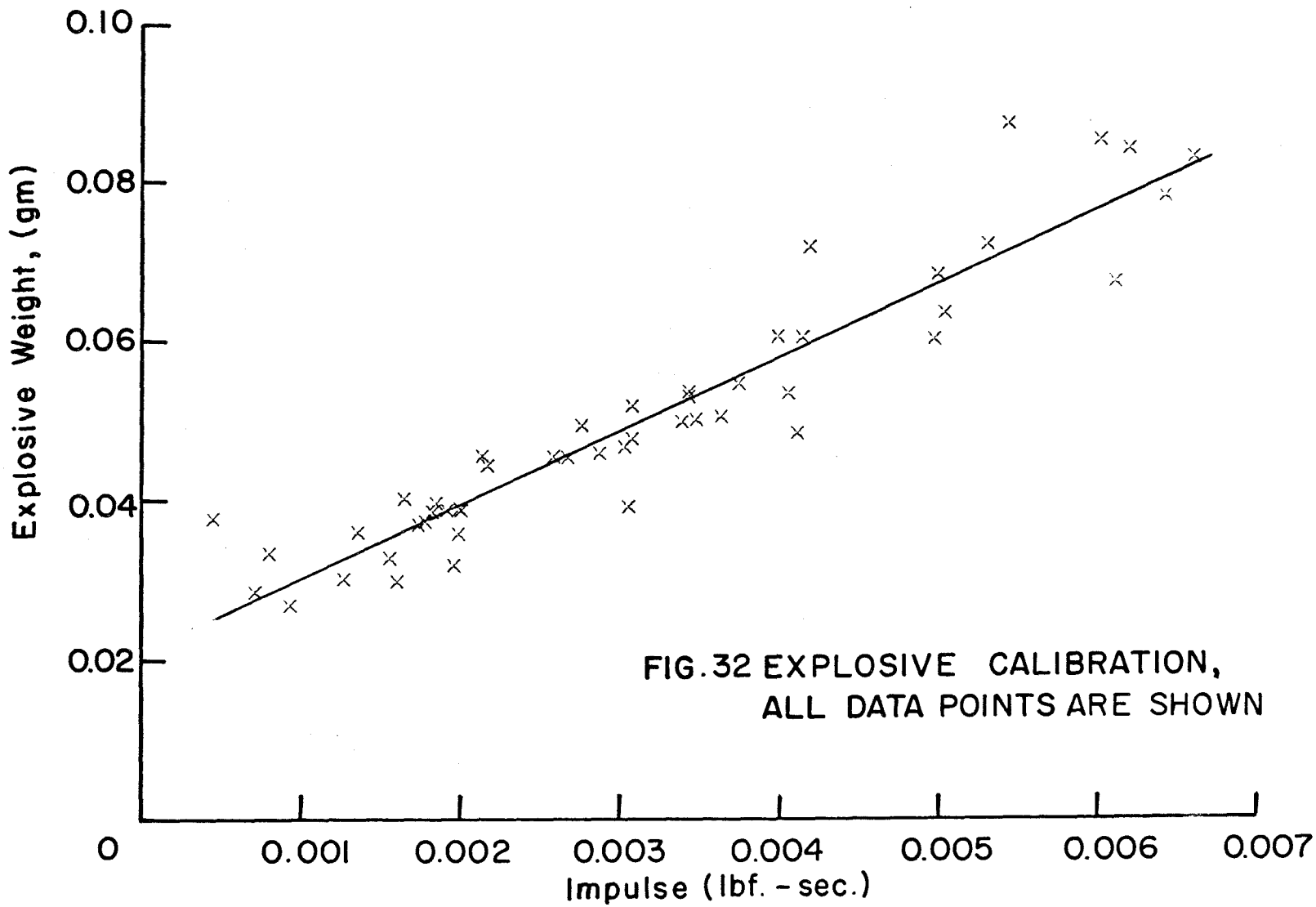

FIG. 32 EXPLOSIVE CALIBRATION,
ALL DATA POINTS ARE SHOWN

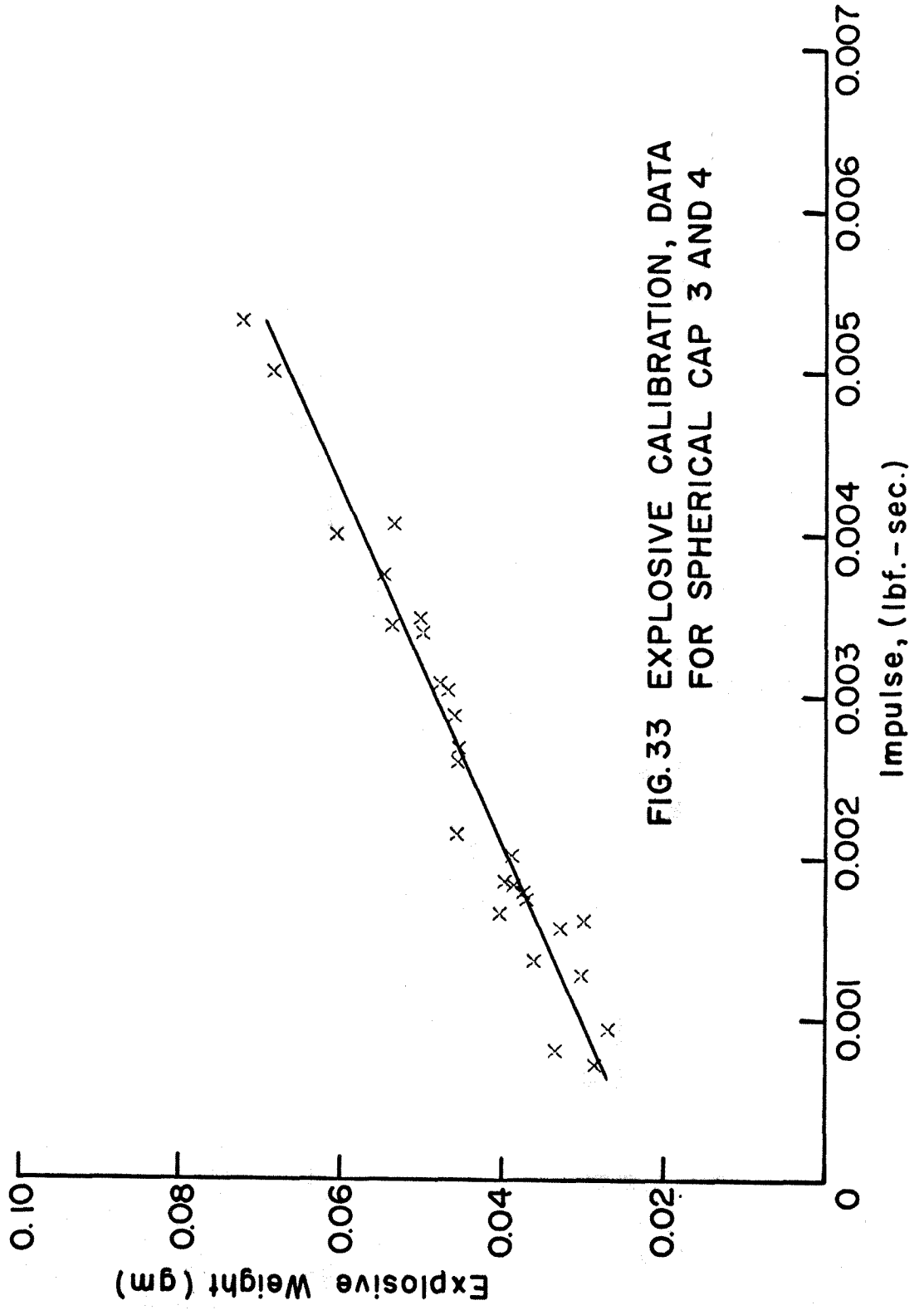

FIG. 33 EXPLOSIVE CALIBRATION, DATA FOR SPHERICAL CAP 3 AND 4

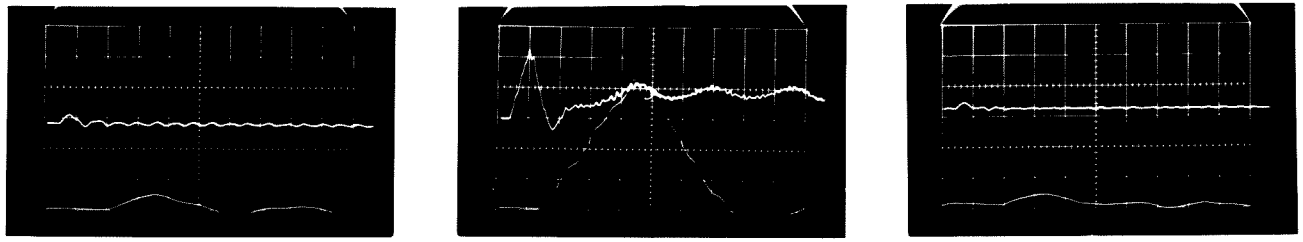

A. Cap 1, p = 7, I_p =.003076 B. Cap 1, p = 7, I_p =.004603 C. Cap 2, p=10, I_p =.003468

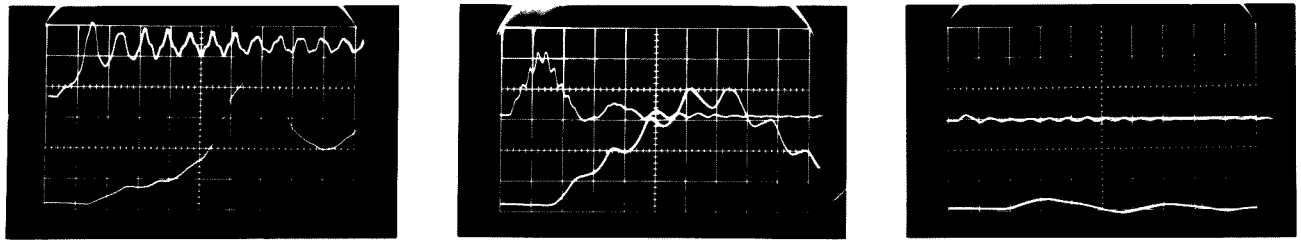

D. Cap 2, p = 10, I_p=.004243 E. Cap 3, p=4, I_p=.005127 F. Cap 3, p=5, I_p=.001723

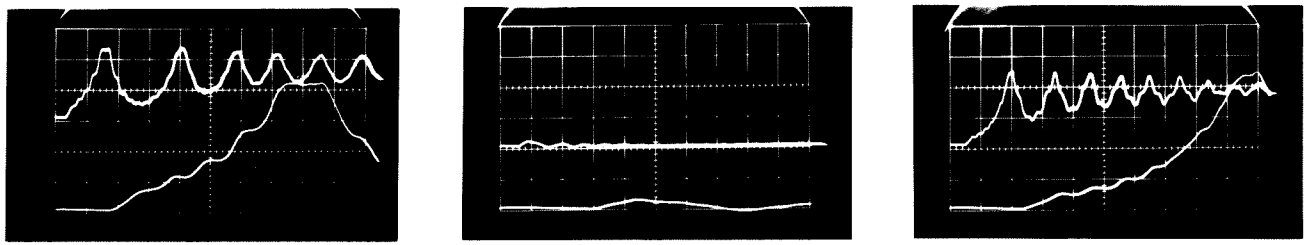

G. Cap 3, p=5, I_p=.00265 H. Cap 4, p=3.5, I_p=.001276 I. Cap 4, p=3.5, I_p=.001919

p = Static Load, psi ; I_p = Impulse of Pendulum, lbf. – sec.

FIG. 34 DISPLACEMENT TIME HISTORY

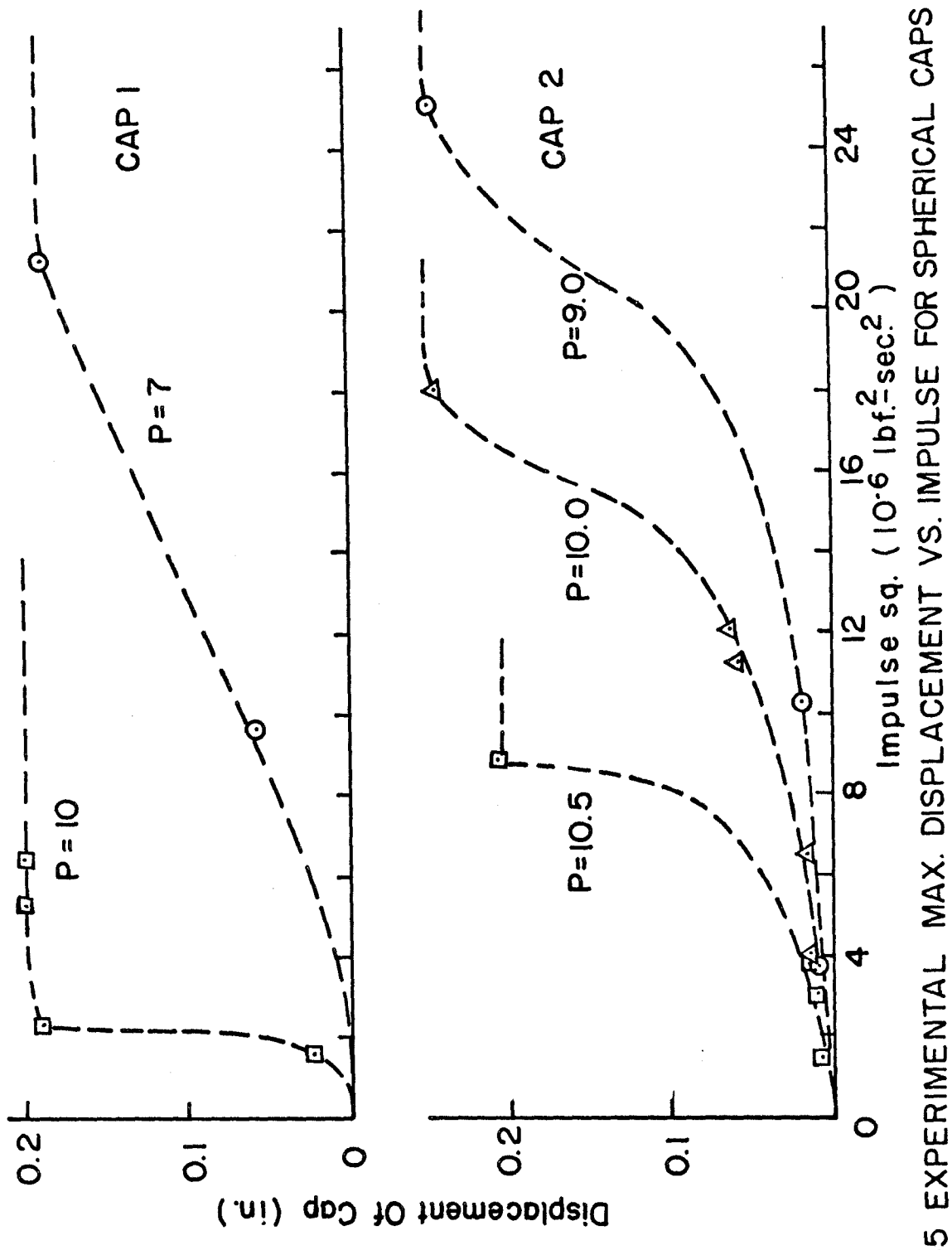

FIG. 35 EXPERIMENTAL MAX. DISPLACEMENT VS. IMPULSE FOR SPHERICAL CAPS 1 & 2

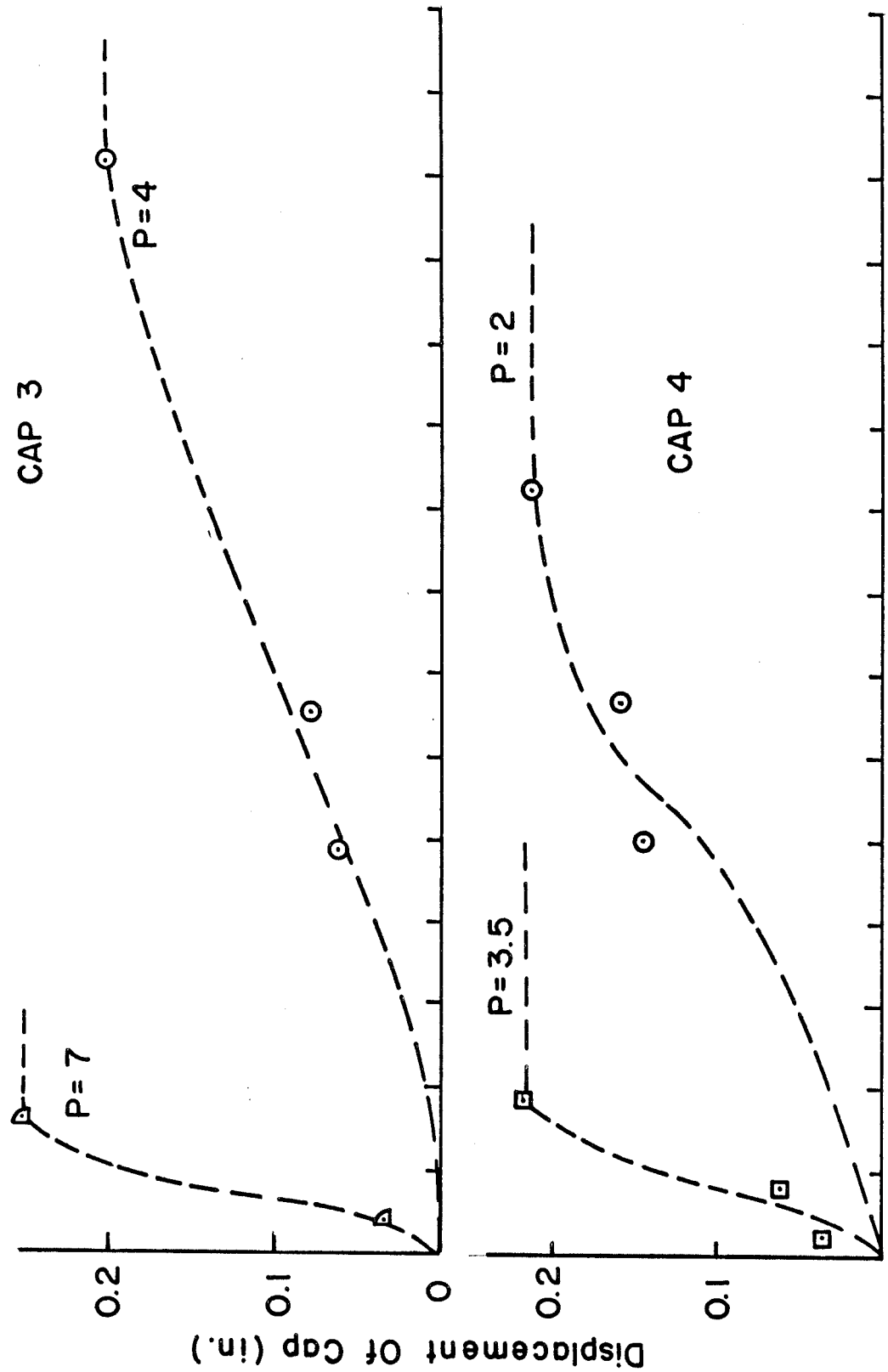

FIG.36 EXPERIMENTAL MAX. DISPLACEMENT VS. IMPULSE FOR SPHERICAL CAPS 3 & 4

FIG. 37 THEORY AND EXPERIMENT FOR SPHERICAL CAP I

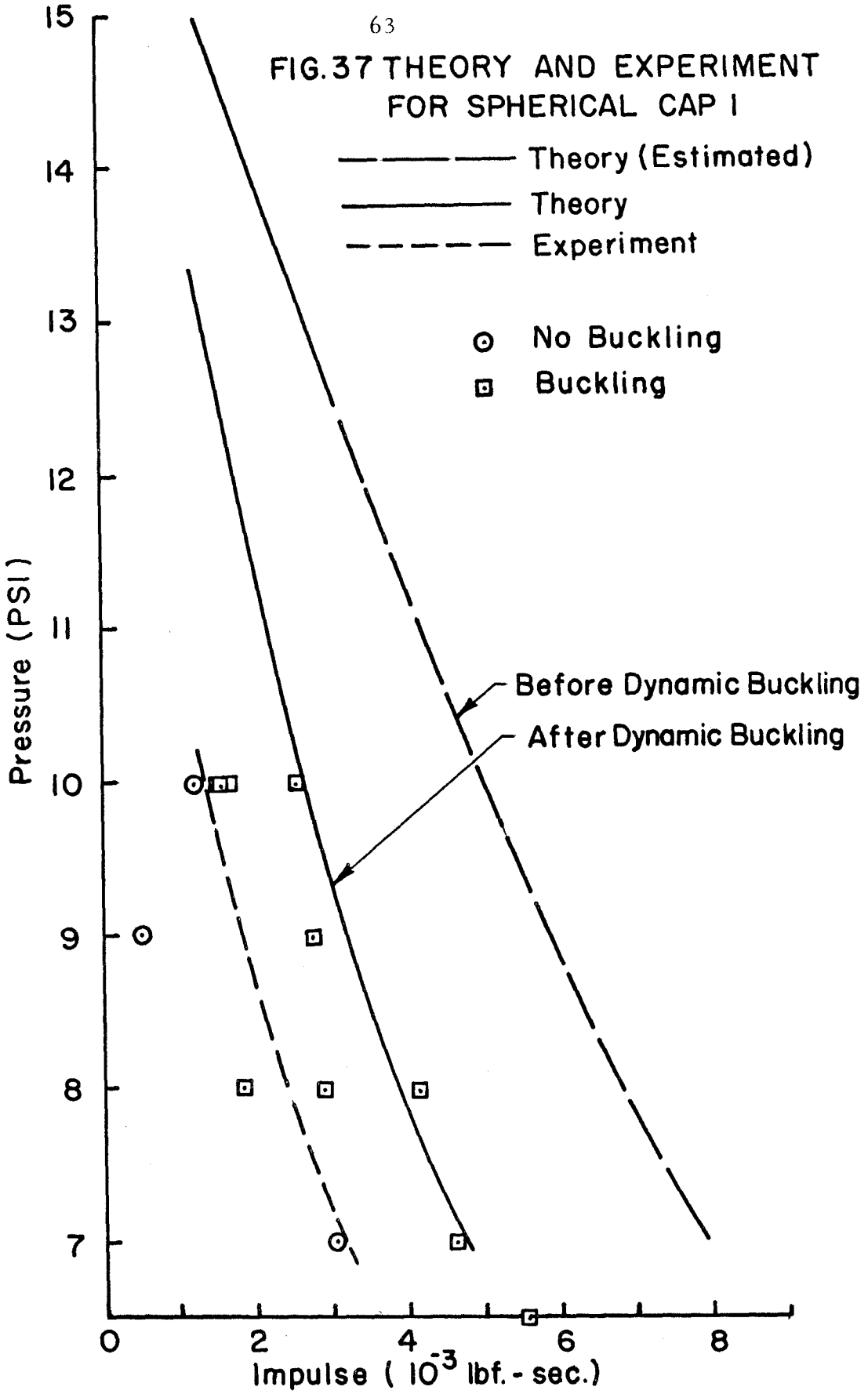

FIG. 38 THEORY AND EXPERIMENT FOR SPHERICAL CAP 2

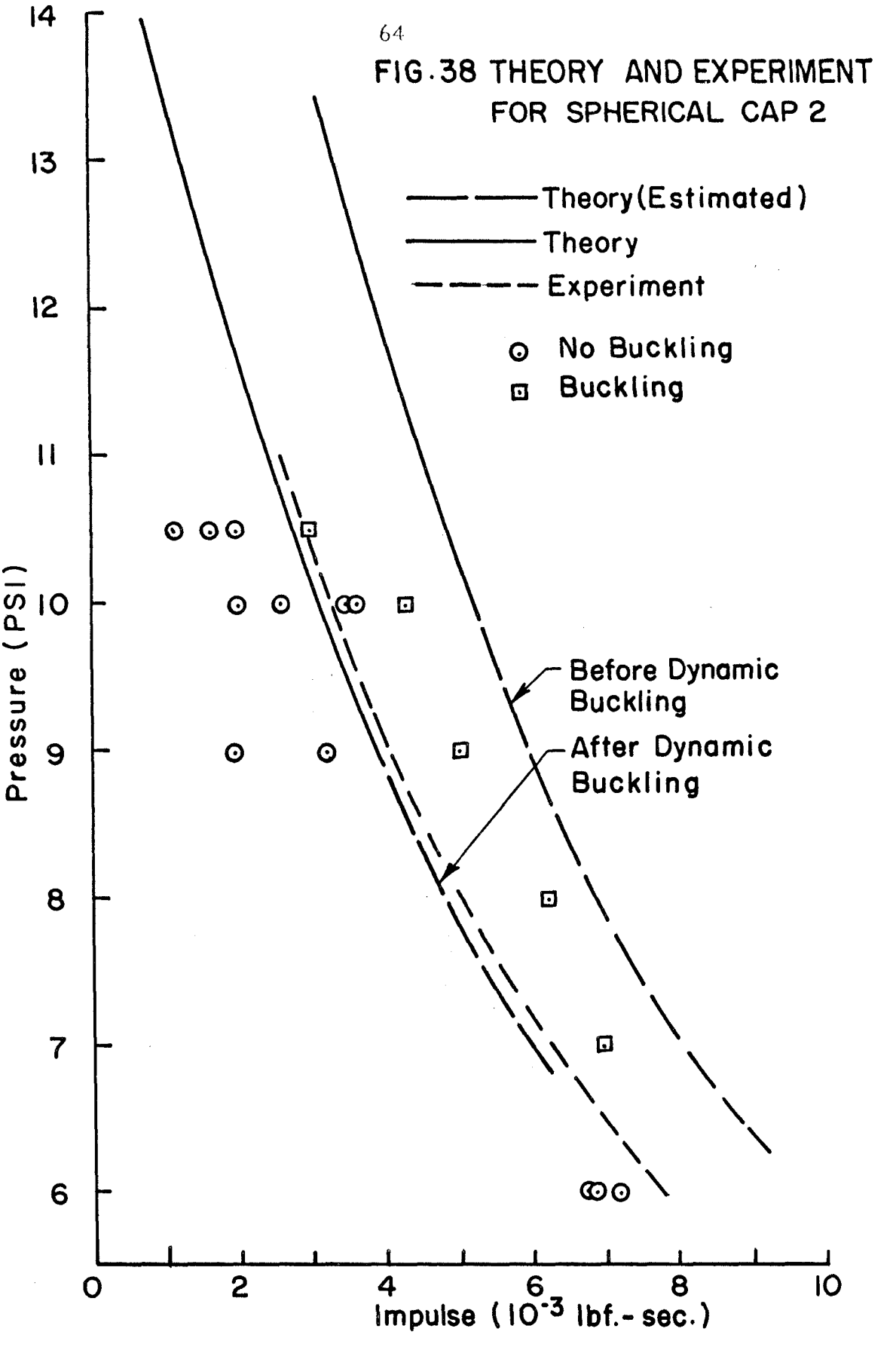

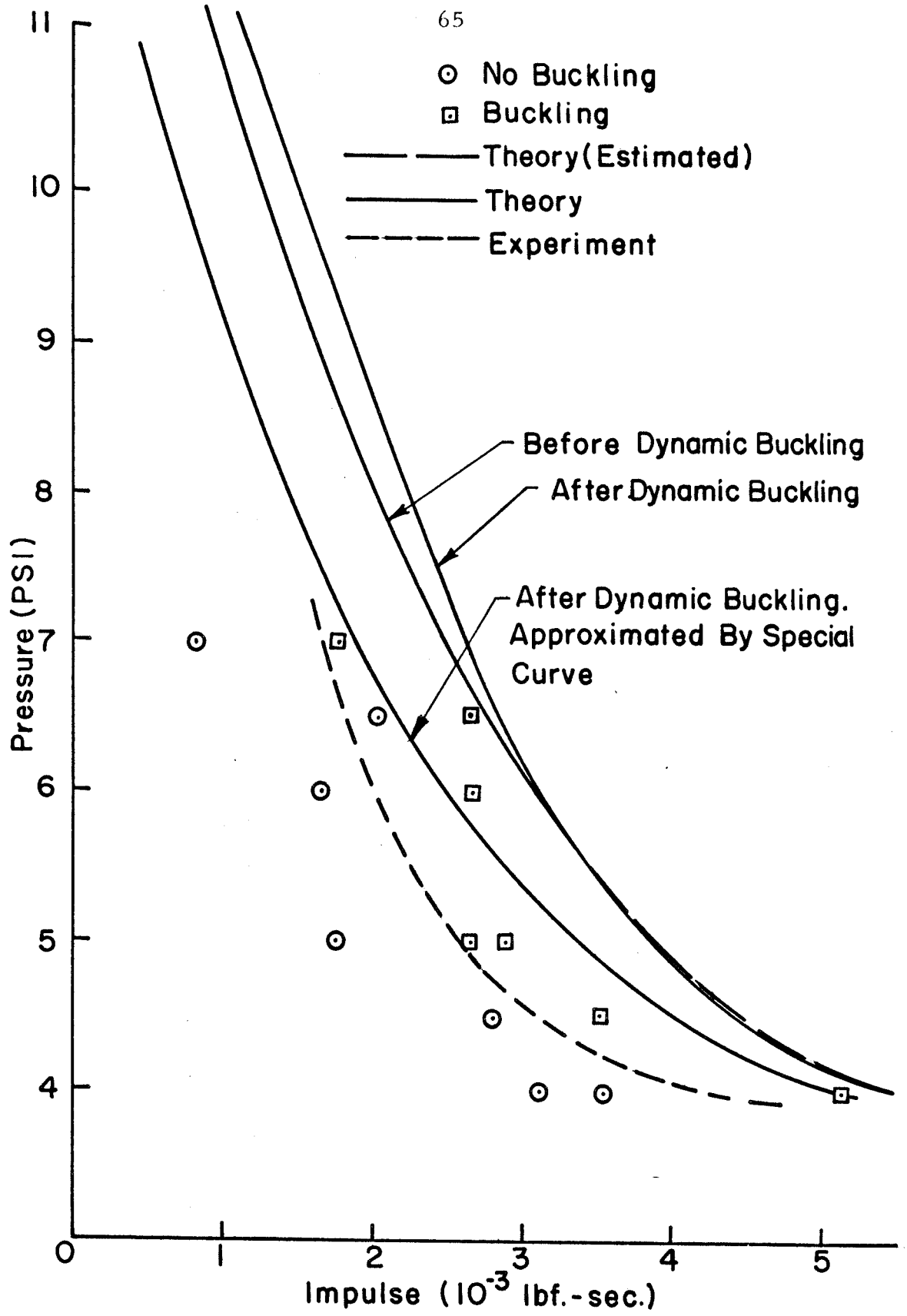

FIG. 39 THEORY AND EXPERIMENT FOR SPHERICAL CAP 3

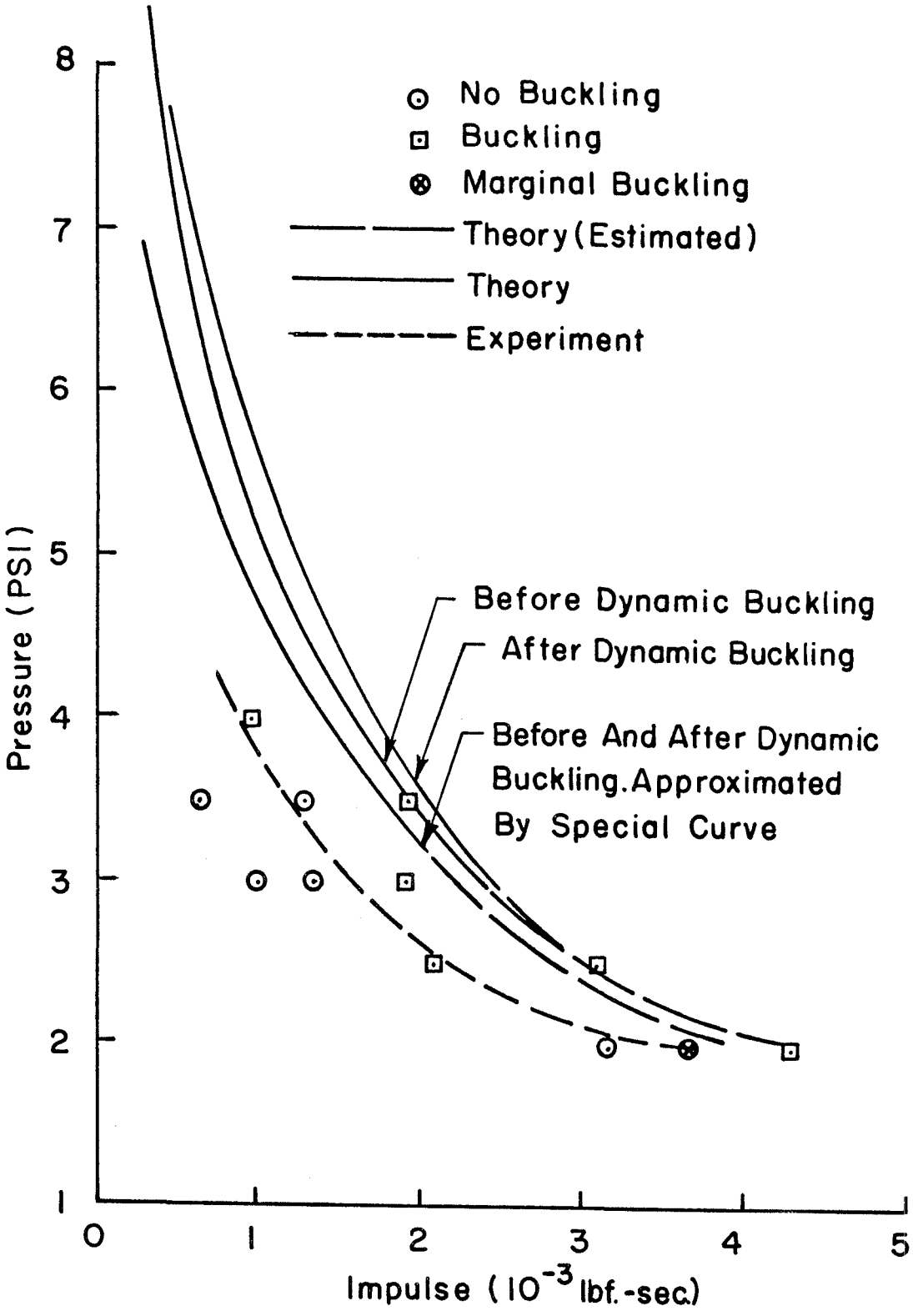

FIG. 40 THEORY AND EXPERIMENT FOR SPHERICAL CAP 4